

Simulation of Heat Conduction in Complex Domains of Multi-material Composites using a Meshless Method

Naman Bartwal^a, Shantanu Shahane^b, Somnath Roy^{a1}, Surya Pratap Vanka^c

^a*Department of Mechanical Engineering
Indian Institute of Technology Kharagpur
Kharagpur, West Bengal 721302*

^b*Google, 1600 Amphitheatre Parkway
Mountain View, California 94043*

^c*Department of Mechanical Science and Engineering
University of Illinois at Urbana-Champaign
Urbana, Illinois 61801*

Abstract

Several engineering applications involve complex materials with significant and discontinuous variations in thermophysical properties. These include materials for thermal storage, biological tissues with blood capillaries, etc. For such applications, numerical simulations must exercise care in not smearing the interfaces by interpolating variables across the interfaces of the sub-domains. In this paper, we describe a high accuracy meshless method that uses domain decomposition and cloud-based interpolation of scattered data to solve the heat conduction equation in such situations. The polyharmonic spline (PHS) function with appended polynomial of prescribed degree is used for discretization. A flux balance condition is satisfied at the interface points and the clouds of interpolation points are restricted to be within respective

¹Corresponding Author Email: somnath.roy@mech.iitkgp.ac.in

domains. Compared with previously proposed meshless algorithms with domain decomposition, the cloud-based interpolations are numerically better conditioned, and achieve high accuracy through the appended polynomial. The accuracy of the algorithm is demonstrated in several two and three dimensional problems using manufactured solutions to the heat conduction equation with sharp discontinuity in thermal conductivity. Subsequently, we demonstrate the applicability of the algorithm to solve heat conduction in complex domains with practical boundary conditions and internal heat generation. Systematic computations with varying conductivity ratios, interpoint spacing and degree of appended polynomial are performed to investigate the accuracy of the algorithm.

Keywords: Meshless method, Polyharmonic splines, Multiple domains, Thermal conductivity, Heat conduction

1. Introduction

In several heat transfer engineering applications, thermal properties such as conductivity, specific heat and density vary discontinuously and significantly across regions of complex shape. Some examples are composite materials, metal foams with embedded polymers for thermal storage and biological tissues embedded with blood vessels [1–3]. In some applications, the thermal properties can vary by as much as a factor of one hundred between adjacent regions. In such situations, while seeking numerical solutions, it is necessary to discretize the governing equations carefully to avoid smearing of the discontinuities as well as prevent non-monotonic variation of the thermal variables. Such regions can be identified and discretized individually

as separate domains with local properties within each region. The unstructured finite volume method is a popular numerical technique used for such problems. However, its accuracy is typically limited to second order unless complex reconstruction schemes or higher order basis functions are used [4–6]. Further, reconstruction schemes and high order basis functions must not interpolate across the discontinuous property interfaces. In addition, the grids/volumes generated must not be excessively skewed and the aspect ratio of the elements must be close to unity to avoid loss of accuracy. Achieving high accuracy with finite volume method can be challenging in problems with large and discontinuous variations in properties. In this paper, we describe a high accuracy meshless numerical technique which uses polyharmonic radial basis functions (PHS-RBF) with appended polynomial to interpolate scattered data and solve elliptic partial differential equations encountered in multiphysics simulations. In our recent works [7–11], we have demonstrated the technique for heat conduction and fluid flow problems in several complex geometries and have shown high discretization accuracy whose order increases with the degree of the appended polynomial. Further, we have used a cloud based interpolation, versus global interpolation, to be able to use large numbers of scattered points. The method can be used to simulate thermal transport in large and complex domains with simultaneous refinement in point spacing as well as polynomial degree ($h - p$ refinement). However, when this method is used in a straightforward way for problems with large and discontinuous property variations, significant errors can result because of interpolation across the discontinuities. Therefore, in this work we have extended the algorithm to multiple subdomains with interpolations strictly

within individual homogeneous domains. At the interfaces, flux balance conditions are imposed for the discrete points on the interfaces. In this paper, we investigate the accuracy resulting from such C_1 condition at the interface by considering manufactured (known) solutions. We then apply the method to several heat conduction problems in complex geometries.

Meshless methods offer several advantages over mesh based methods and have been pursued since the early 1990s. Meshless methods based on radial basis function (RBF) interpolations to solve partial differential equations were originally demonstrated by Kansa [12, 13] who used the Hardy multiquadratics [14] to interpolate scattered data. Kansa's original work used global interpolation which is exponentially accurate but suffers from high condition numbers for modest numbers of scattered points. Subsequently, domain decomposition methods have been proposed to reduce the condition number with coupling between the subdomains through overlapping or interface flux balances [15–23]. However, such methods also are not suitable for large problems with need for millions of scattered points to represent a complex domain. In contrast, interpolation within clouds of scattered points maintains the condition number within solvability limits and produces good accuracy. Further, multiquadratics, inverse multiquadratics and Gaussians all require prescription of a shape parameter [24–42] which dictates interpolation accuracy and the condition number of the interpolation coefficient matrix. On the other hand, interpolation with polyharmonic splines (PHS-RBF) does not need a shape parameter, and when appended with polynomial produces interpolation accuracy consistent with the degree of the appended polynomial [7–11, 43–51]. In our recent works [7–11], we had demonstrated high

accuracy in heat conduction and fluid flow computations in several problems with manufactured solutions. These problems were limited to uniform properties in the solution domain and therefore, there were no interfaces that needed special attention in discretization of the derivatives. When the solution domain consists of regions with significant differences in properties, it is necessary to isolate the distinct regions and discretize the derivatives individually in each subregion. This requires point clouds that are limited to the homogeneous regions with common points on the interfaces. Some recent works with such heterogeneous media are by Reutskiy [52], Ahmad et al. [53] and Gholampour et al. [54]. Reutskiy [52] considered heat conduction in irregular two-dimensional domains while Ahmad et al. [53] demonstrated a subdomain RBF technique for geometries containing irregular interfaces with sharp corners. Gholampour et al. [54] on the other hand, considered solution of elasticity problems with irregular interfaces by employing PHS-RBF and appended polynomial for 2D problems. It is worth mentioning here that the spectral element method [55] also decomposes a complex domain into elements and uses Chebyshev polynomial of high degree in each element. At element boundaries, the variable and its first derivative are made continuous. However, the motivation for such elementwise discretization and interface condition in spectral element methods is different from current motivation. When properties are modestly varying across the domain, the current cloud based method does not need special domain decomposition, unless needed for parallel computing purposes.

Section 2.1 of this paper first briefly describes the PHS-RBF technique for single domains with homogeneous properties. In section 2.2, we present

details of the extension of this algorithm to problems with regions of discontinuous and significant property variations. The accuracy of the multidomain algorithm is then evaluated by comparing it with the smearing approach as discussed in section 3. A detailed convergence analysis is presented in section 4. Subsequently, in section 5, we apply the algorithm to more practical problems. Section 6 provides summary of current observations and plans for future work.

2. Methodology

2.1. Single Domain PHS-RBF Algorithm

In this section, we first briefly describe the single domain cloud-based PHS-RBF algorithm to solve heat conduction and fluid flow problems in complex geometries. As this technique has been documented in our recent works [7–11], as well as of some others [43–49], we describe the details only briefly for completeness and relevance to the multidomain algorithm. The starting point for the algorithm is the layout of scattered points in the complex solution domain. These scattered points can be generated by any of the techniques [56–59] including the vertices of any finite element grid generated by standard software. While the latter practice may appear as grid generation, it is to be mentioned that the elements and edges are eventually removed and thus, there are no issues of element skewness or aspect ratio which degrade the discretization accuracy. The second step is the definition of clouds for interpolation of neighbor values. For each scattered point, a subset of the nearest neighbor points is defined based on the degree of the appended polynomial. For a polynomial of degree p and dimension of the

problem d , the number of cloud points is given by $2\binom{p+d}{p}$. When the scattered point does not have enough interpolation points on one side, the cloud is extended in other directions asymmetrically. This happens near the external boundaries, or internal obstacles. For each scattered point, a separate cloud is defined. Figure 1 shows a typical base point denoted by a green star and its cloud.

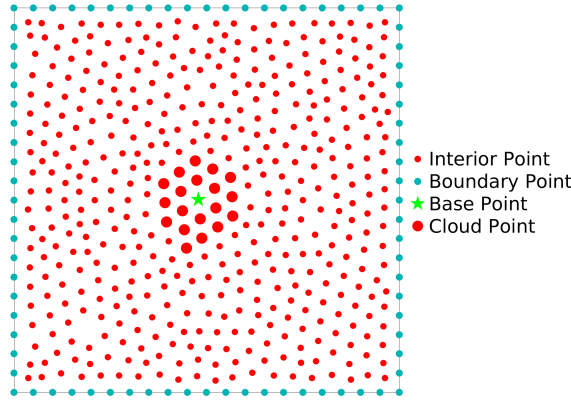


Figure 1: Methodology: Scattered distribution of points within a domain and example of a cloud.

The next step is computation of interpolation weights. For this interpolation, we use the PHS with appended polynomial as

$$s(\mathbf{x}) = \sum_{i=1}^q \lambda_i \phi(\|\mathbf{x} - \mathbf{x}_i\|_2) + \sum_{i=1}^m \gamma_i P_i(\mathbf{x}) \quad (1)$$

where, $\phi(\|\mathbf{x} - \mathbf{x}_i\|_2)$ indicates polyharmonic spline radial basis function (PHS-RBF) and $\|\mathbf{x} - \mathbf{x}_i\|_2$ is the distance between the location at which the function s is approximated (green coloured star shaped dot in fig. 1) and different data points in its cloud (enlarged red coloured circular dots in fig. 1).

λ_i and γ_i are weights given to the PHS-RBF kernel and the appended monomials P_i , respectively. The PHS function ϕ is given as $\phi = (\|\mathbf{x} - \mathbf{x}_i\|_2)^{2\alpha+1}$, where α is a positive integer. If the values of s are known at the scattered points, the above interpolation can be evaluated by collocating the data at the scattered points and thus providing a formula to evaluate $s(\mathbf{x})$ at any intermediate location. Let \mathcal{L} be any linear differential operator of the governing partial differential equation. Applying \mathcal{L} to eq. (1) and collocating at the q cloud points gives q equations. The number of cloud points q is taken to be twice the number of monomials, giving the total number of unknowns to be $(q + m)$. The additional m equations for λ are given by the constraints

$$\sum_{i=1}^q \lambda_i P_j(\mathbf{x}_i) = 0 \quad \text{for } 1 \leq j \leq m \quad (2)$$

Above collocation and constraint [7] written together in the matrix-vector form gives:

$$\mathcal{L}[\mathbf{s}] = \left(\begin{bmatrix} \mathcal{L}[\Phi] & \mathcal{L}[\mathbf{P}] \end{bmatrix} \begin{bmatrix} \mathbf{A} \end{bmatrix}^{-1} \right) \begin{bmatrix} \mathbf{s} \\ \mathbf{0} \end{bmatrix} \quad (3)$$

$$\text{where } \begin{bmatrix} \mathbf{A} \end{bmatrix} = \begin{bmatrix} \Phi & \mathbf{P} \\ \mathbf{P}^T & \mathbf{0} \end{bmatrix} \quad (4)$$

is a matrix of geometric values and monomials evaluated at the scattered points. The inverse of matrix \mathbf{A} in eq. (4) is written only as a mathematical notation. In practice, a linear solver is used. Equation (3) can be further

simplified as

$$\mathcal{L}[\mathbf{s}] = [\mathbf{B}] \begin{bmatrix} \mathbf{s} \\ \mathbf{0} \end{bmatrix} = [\mathbf{B}_1][\mathbf{s}] + [\mathbf{B}_2][\mathbf{0}] = [\mathbf{B}_1][\mathbf{s}] \quad (5)$$

$[\mathbf{B}_1]$ is of size $(q \times q)$ and contains coefficients for the linear differential operators such as gradient, Laplacian, etc. $[\mathbf{B}_1]$ depends only on the geometric distances between the individual points and its cloud points. Equation (5) is satisfied at each one of the scattered points, generating a row of coefficients in the assembled matrix. This sparse coefficient matrix is of size $n \times n$ with q non-zero coefficients in each row. The sparse equation set is then solved for the unknown discrete values s_i , $i = 1$ to n . In this work, we have used a preconditioned BiCGSTAB [60], although other solvers such as multilevel methods [50] can also be used. The above single domain algorithm was applied to several heat conduction problems in [9] and was shown to achieve high accuracy. By considering different point spacings, we have shown that the discretization accuracy varies (in case of Laplacian) approximately as one order less than the degree of the appended polynomial and of the same order as the polynomial degree in case of gradients [7]. However, if there are regions of significant and distinct variations in thermal properties, such accuracy can be lost. Consider the solution of the steady state heat conduction equation with a source term in a two dimensional space:

$$\frac{\partial}{\partial x} \left(k \frac{\partial T}{\partial x} \right) + \frac{\partial}{\partial y} \left(k \frac{\partial T}{\partial y} \right) = \dot{q} \quad (6)$$

Equation (6) can be discretized either by first discretizing $k \frac{\partial T}{\partial x}$ and $k \frac{\partial T}{\partial y}$ and

then taking their derivatives again or by expanding the derivatives as

$$k \left(\frac{\partial^2 T}{\partial x^2} + \frac{\partial^2 T}{\partial y^2} \right) + \frac{\partial k}{\partial x} \frac{\partial T}{\partial x} + \frac{\partial k}{\partial y} \frac{\partial T}{\partial y} = \dot{q} \quad (7)$$

In the above expansion, we can then evaluate the first and second derivatives using the kernel differentiation procedure explained above. The \mathbf{B}_1 matrix mentioned in eq. (5) now contains the coefficients from the Laplacian and from the first derivatives of the temperature (T). The sharp discontinuity in the conductivity is manifested by the derivatives $\frac{\partial k}{\partial x}$ and $\frac{\partial k}{\partial y}$, which needs to be evaluated using the RBF first derivative matrix. Although, the analytical derivatives of this step function do not exist, the RBF computes it using the stencil for the first derivative, much like computing a derivative across a shock in shock capturing techniques. We have evaluated this procedure by solving for a manufactured solution with two regions of distinct conductivity. Three ratios of the thermal conductivities $\frac{k_L}{k_{II}} = 5, 10$ and 100 with different point spacings and degree of the appended polynomial were considered. We show the results for two different problems: (a) circle inside a square (fig. 2) and (b) astroidal domain inside a square (fig. 4). Figures 3 and 5 show the temperature contours for the interior and boundary conditions given by eq. (8).

$\dot{q} = 100$ at every node inside the circular and astroidal domain (blue dots)

$T = 0$ at the rectangular boundary (cyan dots)

$k = 10$ (red and cyan dots) and $k = 1$ (blue dots)

(8)

For conductivity ratio of 10, we see that the single domain technique which

interpolates the temperatures and conductivities through the interface, significantly smears the discontinuity and results in erroneous results as shown by the contours of non-dimensional temperature (figs. 3 and 5). The larger the polynomial, the bigger is the cloud, and generates larger errors contrary to the expected higher accuracy.

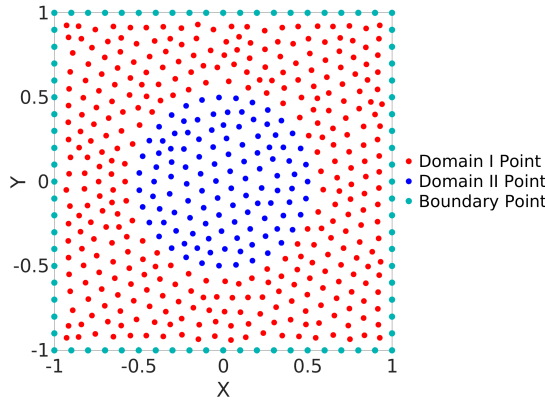


Figure 2: Methodology: Distribution of 531 scattered points within a domain with two regions of dissimilar conductivity.

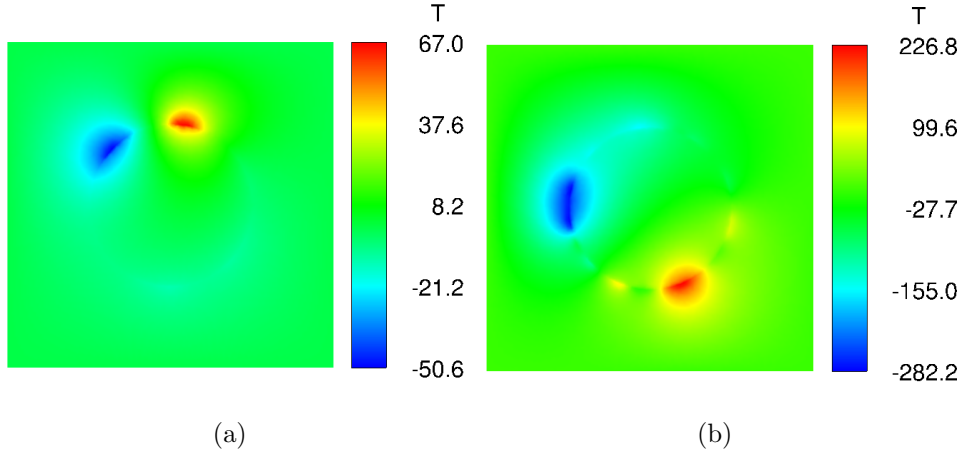


Figure 3: Methodology: Temperature contours (a) polynomial degree = 3 and (b) polynomial degree = 5 for 12078 scattered points.

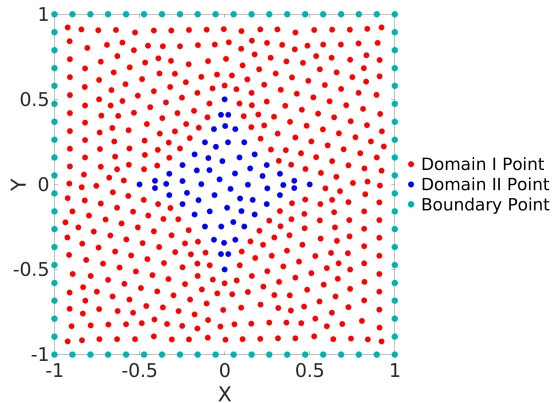


Figure 4: Methodology: Distribution of 540 scattered points within a domain with two regions of dissimilar conductivity.

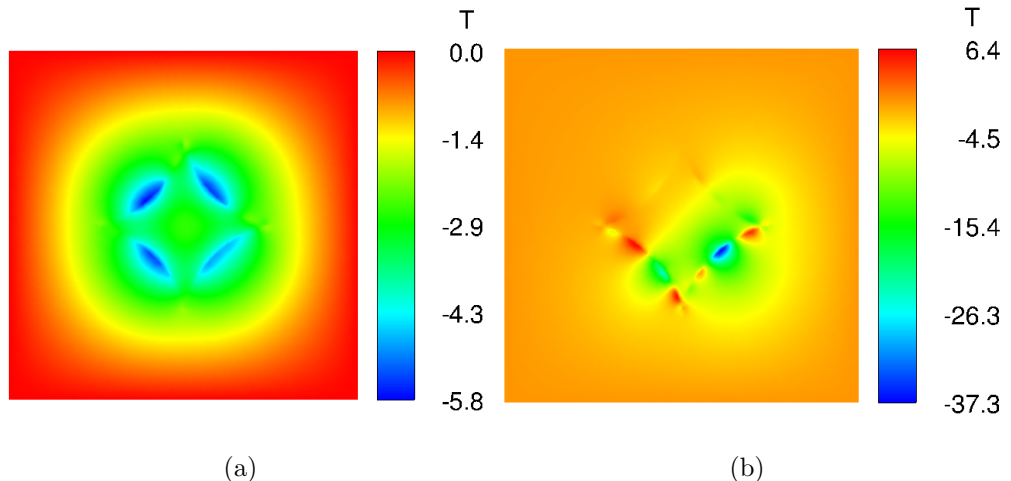


Figure 5: Methodology: Temperature contours (a) polynomial degree = 3 and (b) polynomial degree = 5 for 12060 scattered points.

2.2. Algorithm for Multiple Domains

As shown above, interpolation across the interfaces results in large errors and destroys the high spatial accuracy observed for domains with homogeneous thermal properties. This is because the clouds are defined isotropically that leads to interpolations through the interfaces. It is obvious that the heterogeneous regions should be isolated and separately interpolated and treated as separate subdomains. This is similar to the well-known shock patching techniques used in computation of high-speed gas dynamics problems. In this section, we describe the multidomain technique with the cloud based PHS-RBF interpolation. The verification and accuracy of the technique for several problems with manufactured solutions are then demonstrated followed by applications of the algorithm to two and three dimensional heat conduction in complex geometries.

The algorithm again begins with the layout of scattered points in the solution domain. However, we first define the interfaces separating the various regions, and layout scattered points on the interfaces. For 2D problems, we layout points along the line interfaces. For 3D problems, we first triangulate the surfaces of the interfaces, and remove the edges and elements. Then, using these interface points and the points prescribed on the external boundaries, we generate separate sets of points in all the subdomains. As before, the points can be vertices of elements of a finite element grid. The governing heat conduction equation is then individually satisfied in each subdomain, without any interpolation across the domains. On the interface, the partial differential equation is not satisfied. Instead, we impose the C_0 and C_1 conditions at each of the interface points. Thus, for all the interface points the

flux balance condition is satisfied,

$$k_1 \frac{\partial T}{\partial \hat{n}} \Big|_1 = k_2 \frac{\partial T}{\partial \hat{n}} \Big|_2 \quad (9)$$

The C_0 condition is automatically satisfied by the common temperatures at the interface. The next step is the definition of the cloud points. This is where the main difference arises. In the multidomain algorithm, the clouds are defined to contain only points in their own subdomain. Hence near the interfaces, the clouds are defined asymmetrically, thus avoiding interpolation across the interfaces. Figures 6 and 7 show three types of clouds that can result in the simple case of an interface, boundary and interior points for degree of appended polynomial equal to 3.

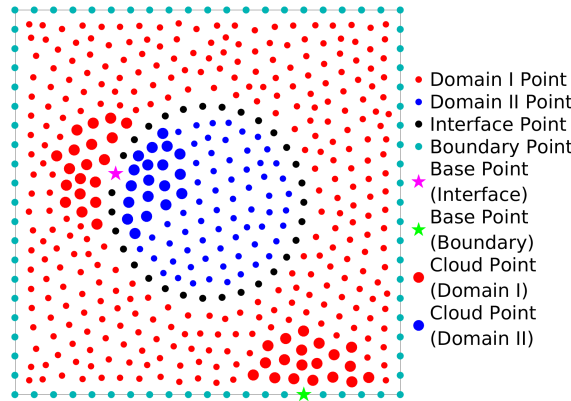


Figure 6: Methodology: Clouds formed by points located at the interface (magenta coloured star shaped dot) and boundary (green coloured star shaped dot) at polynomial degree = 3

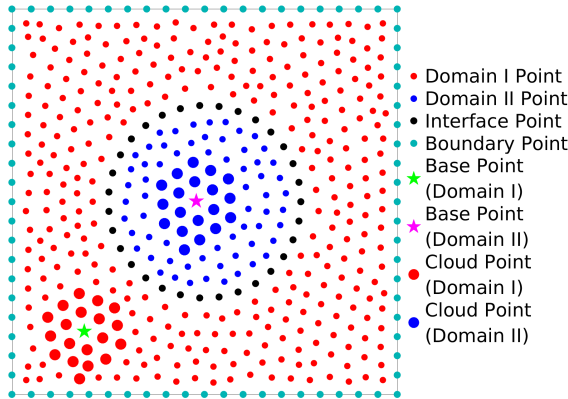


Figure 7: Methodology: Clouds formed by points located in the inner (magenta coloured star shaped dot) and outer domain (green coloured star shaped dot) at polynomial degree = 3

Clouds in the interiors of each subdomain are isotropic if there are enough neighbor points available. If sufficient cloud points are not available, points are picked in the other directions and are restricted to be in their own subdomain as in the case of the external boundaries. A point on the interface has two subdomains on the two sides of its normal. Hence, two sets of cloud points, one in each subdomain are defined. These two clouds are used to compute the normal derivatives and the fluxes on each side using the conductivities in the appropriate subdomain. The flux balance condition at each interface point then gives an additional equation to close the system. The final step in the algorithm is the assembly of the coefficient matrix. We assemble one single coefficient matrix for all subdomains combined. This matrix consists of the satisfaction of the partial differential equation at all interior points in each subdomain and the flux balance condition at all the points on the interfaces. At the external boundaries, based on the type of

boundary condition (Dirichlet or Neumann), we fix the value, or include an implicit equation for the derivative. In such a case, clouds are defined for the points on the external boundaries as well. The total number of discrete equations is therefore the sum of all points interior to the subdomains, points on the interfaces and points on external boundaries. The number of discrete equations equals the number of discrete unknowns, making the problem well posed. As before, we solve the set of equations using a preconditioned BiCGSTAB algorithm, after reorganizing the matrix using the well known reverse Cuthill-McKee (RCM) algorithm [61] which reduces the bandwidth of the sparse matrix.

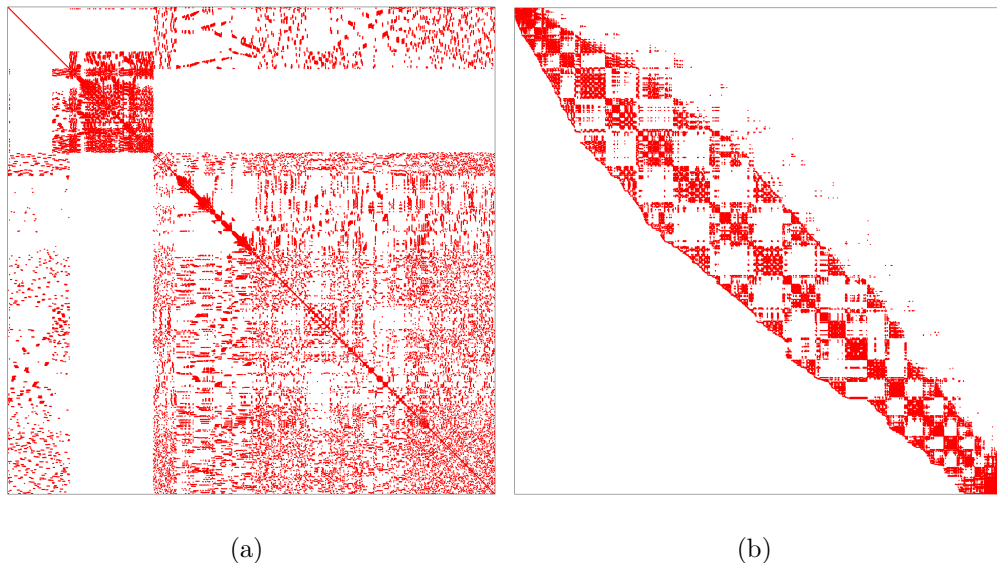


Figure 8: Methodology: Sparsity pattern of the final coefficient matrix for the multidomain algorithm with 1541 points: (a) before RCM and (b) after RCM

Figure 8 shows the sparsity of the final assembled matrix before and after the application of RCM for 1541 scattered distribution of points within the

domain. In summary, the multidomain algorithm differs from our previously published single domain algorithm in the following steps:

- (a) The scattered points are generated separately for each subdomain after deciding the points on the interior interfaces.
- (b) The clouds for each scattered point in the interior of the subdomains are defined so as to include only points within the subdomain (together with the interface points) and not to include points across the interfaces.
- (c) The governing partial differential equation is satisfied only at the points interior to the subdomains and not on the interfaces.
- (d) At points on the interfaces, flux balance equations are satisfied using two sets of clouds spanning into the two adjacent domains along the local normal.

Note that normals at each scattered point on the interface are required for the flux balances. These normals are precomputed at the time of point generation from information of the finite element grid before deleting the elements and edges. Figure 9 shows the steps adopted for multidomain algorithm in the form of a flowchart. In the following sections we validate the algorithm and evaluate the order of accuracy for different conductivity ratios in two and three dimensional problems. We then apply the algorithm to compute heat conduction in complex composite material configurations.

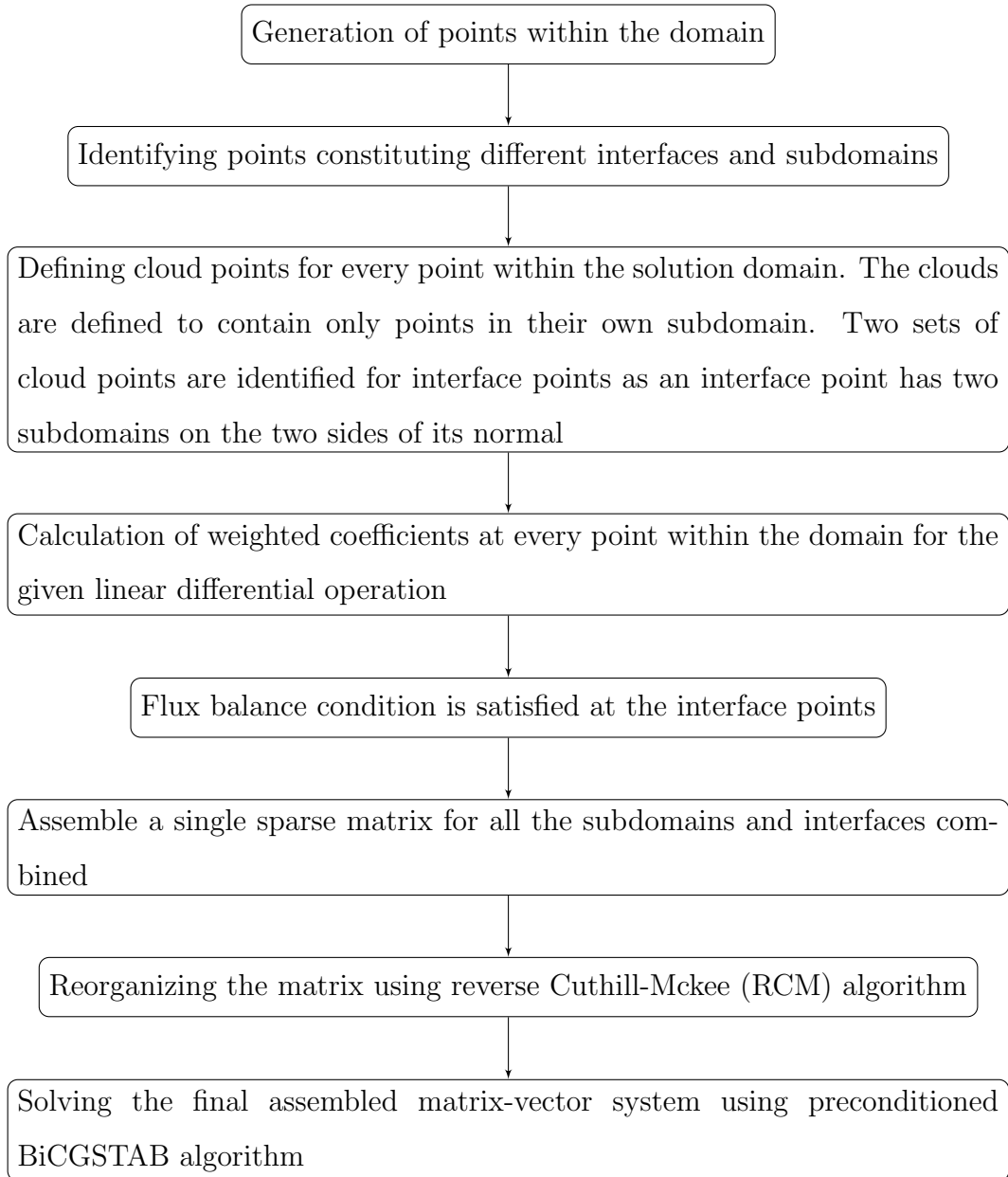


Figure 9: Flowchart showing steps adopted for multidomain algorithm.

3. Verification

In this section, we verify the implementation of the multidomain algorithm by considering a problem of equal thermal conductivities in two sub-domains. An artificial circular domain is separated by distinct scattered points and the results of the single and multidomain algorithms are compared. In the multidomain algorithm, an interface is also defined at which the differential equation is not satisfied but the flux is balanced. Figure 10 shows the distribution of 531 points within the domain (Red dots → Domain I, Blue dots → Domain II and Black dots → Interface). Open source software Gmsh [56] is used to generate the points by the technique of Delaunay triangulation.

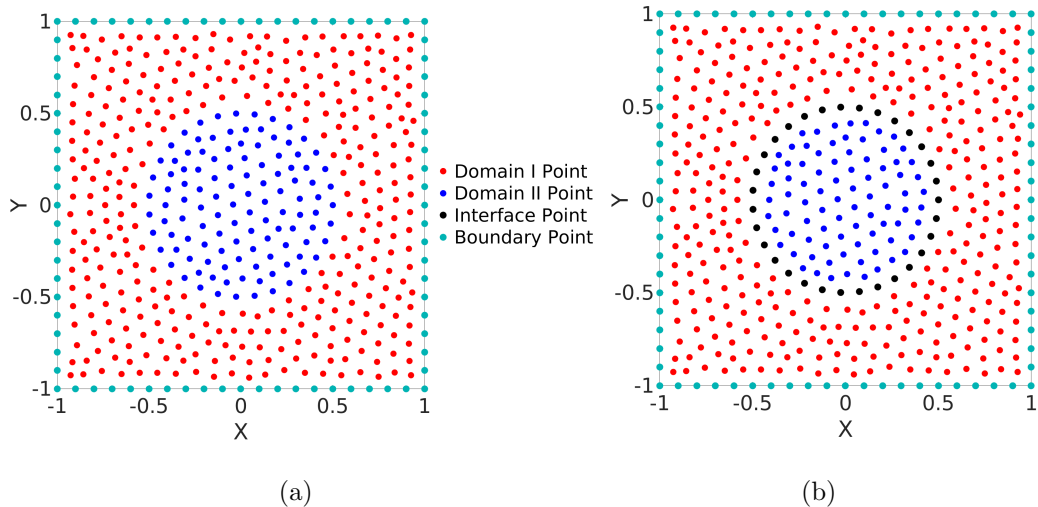


Figure 10: Verification: Point distributions (a) without and (b) with an explicit interface.

We consider equal thermal conductivities in domain I and domain II. We take two different scenarios. In the first one as shown in fig. 10(a), there is no interface and the cloud of a particular point is not limited to its respective

subdomain but may contain points from other domain. In the second case, as depicted by fig. 10(b), the cloud is restricted to individual subdomains, and the flux conditions are satisfied at the interface points. As the thermal conductivities are equal in the subdomains, we must get comparable results using both the approaches. We solve the heat conduction equation for a manufactured solution for temperature given by:

$$\begin{aligned} T_I &= k_I \sin(x^2 + y^2 - r^2) \\ T_{II} &= k_{II} \sin(x^2 + y^2 - r^2) \end{aligned} \quad (10)$$

where, radius of circular domain $r = 0.5$. A surface plot of the manufactured temperature distribution is shown in fig. 11.

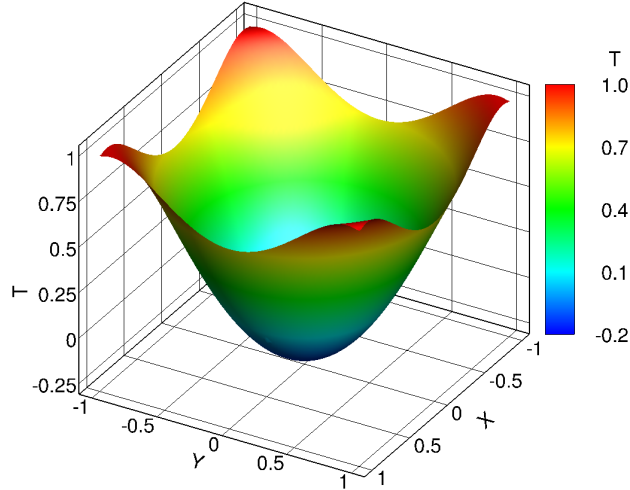


Figure 11: Verification: Surface plot of the manufactured temperature distribution.

Four different point distributions with 1541, 3089, 6033 and 12078 points having an average inter-point spacing of 0.052, 0.037, 0.027 and 0.019 are considered and the degree of appended polynomial is varied from 3 to 6.

Figure 12 shows the log-log variation of L1-norm of the discretization error with respect to average grid spacing for both the strategies of defining the clouds. The closest node is identified for every point and the average of these distances is defined as Δr .

The error for the entire domain given as

$$Error_{Domain} = \frac{\sum_{n=1}^N |T_{exact} - T_{calc}|}{|T_{max_exact}| \times N} \quad (11)$$

where, N is the number of points in the combined domain, T_{exact} , T_{calc} and T_{max_exact} are the manufactured solution, computed solution and the maximum exact value, respectively. The order of convergence is approximately determined by a line of best fit. We show that the two approaches give the expected order of convergence for a given degree of appended polynomial. This verifies the domain decomposition algorithm to produce accurate results and verifies the implementation of the flux balance condition.

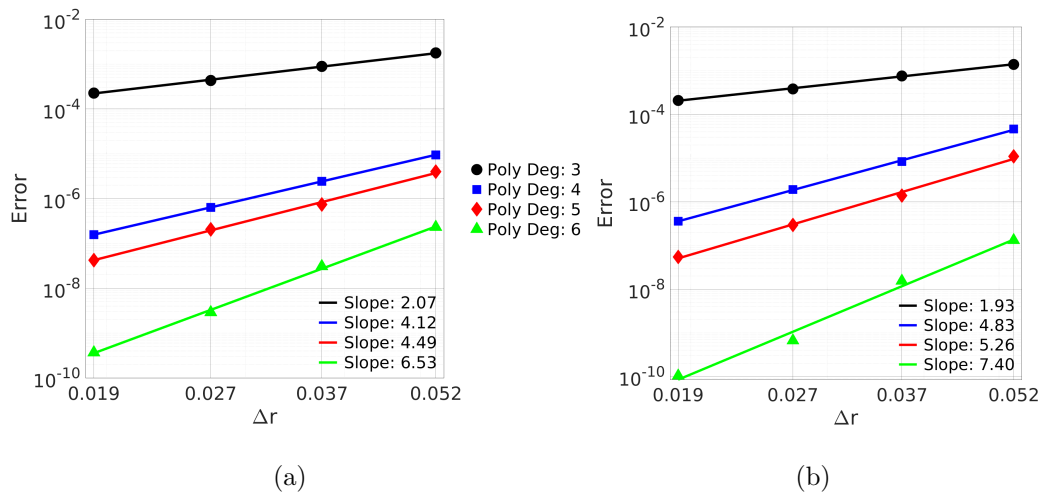


Figure 12: Verification: Variation of error with average point spacing for (a) single domain and (b) multi domain calculations with equal conductivities.

4. Study of Multidomain Accuracy with Manufactured Solutions

In this section, we apply the multidomain algorithm to study the robustness and accuracy in two and three dimensional geometries, all with manufactured solutions. The geometries are: (i) circle inside a square (ii) astroidal domain inside a square and (iii) sphere inside a cube. For each case, the solution domain is divided into domain I, domain II and an interface. Each problem is investigated for three thermal conductivity ratios of 5, 10 and 100. Non-dimensional errors in the computed temperatures are estimated using the manufactured solutions as follows:

$$Error_I = \frac{\sum_{n=1}^{N_I} |T_{exact} - T_{calc}|}{(|T_{exact_max_I} - T_{exact_min_I}|) \times N_I} \quad (12)$$

$$Error_{II} = \frac{\sum_{n=1}^{N_{II}} |T_{exact} - T_{calc}|}{(|T_{exact_max_II} - T_{exact_min_II}|) \times N_{II}} \quad (13)$$

$$Error_{Interface} = \frac{\sum_{n=1}^{N_{Int}} |T_{exact} - T_{calc}|}{\frac{|T_{exact_max_I} - T_{exact_min_I}| + |T_{exact_max_II} - T_{exact_min_II}|}{2} \times N_{Int}} \quad (14)$$

Here, N_I , N_{II} and N_{Int} are the number of points in domain I, domain II and the interface, respectively.

4.1. Circle inside a square

We reconsider the problem of circular domain inside a square as discussed in section 3, but now with different thermal conductivities. The manufactured temperature distribution for different subdomains is given by eq. (15)

and is shown in fig. 13 for a conductivity ratio $\frac{k_I}{k_{II}}$ of 10 .

$$\begin{aligned} T_I &= k_{II} \sin(x^2 + y^2 - r^2) \\ T_{II} &= k_I \sin(x^2 + y^2 - r^2) \end{aligned} \quad (15)$$

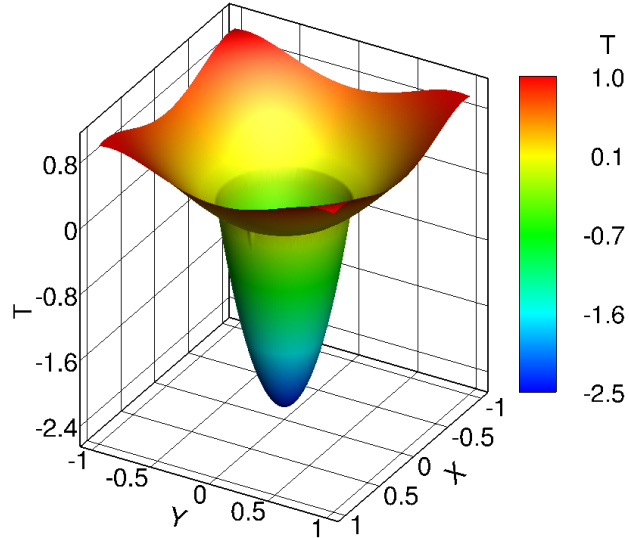


Figure 13: Circle inside a square: Surface plot of the manufactured temperature distribution for circle inside a square and conductivity ratio of 10.

The manufactured temperature distribution (eq. (15)) is designed such that temperature and heat fluxes are both continuous at the interface points. Table 1 lists the total number of points considered for the error analysis and their distributions within domain I, domain II and the interface.

Δr	N	N_I	N_{II}	N_{Int}
0.052	1541	1221	266	54
0.037	3089	2455	556	78
0.027	6033	4817	1106	110
0.019	12078	9674	2247	157

Table 1: Circle inside a square: Average grid spacing (Δr) with the corresponding total number of points distributed within the entire domain (N) and subdomains i.e. Domain I (N_I), Domain II (N_{II}) and Interface (N_{Int}).

Figure 14 presents the discretization error as a function of the average grid spacing for the degrees of appended polynomial varied from 3 to 6 for thermal conductivities ratios of 5, 10 and 100. We have presented the average of errors over the three domains including the interface. It can be seen that for each case, the order of convergence has a minimum value of $k - 1$ for a polynomial degree of k , even for a large conductivity ratio of 100. The rate of convergence increases from 1.91 for polynomial degree of 3 to 6.50 for polynomial degree of 6. Figure 15 shows the variation of the errors in individual domains for a thermal conductivity ratio of 10. It can be seen that all three domains (including the interface) display the expected rate of convergence for a given degree of the appended polynomial. It can be seen from fig. 16 that the errors ($\text{Abs}(\text{Diff}) = |T_{exact} - T_{calc}|$) reduce very fast with increase in degree of appended polynomial, establishing the high accuracy of the method.

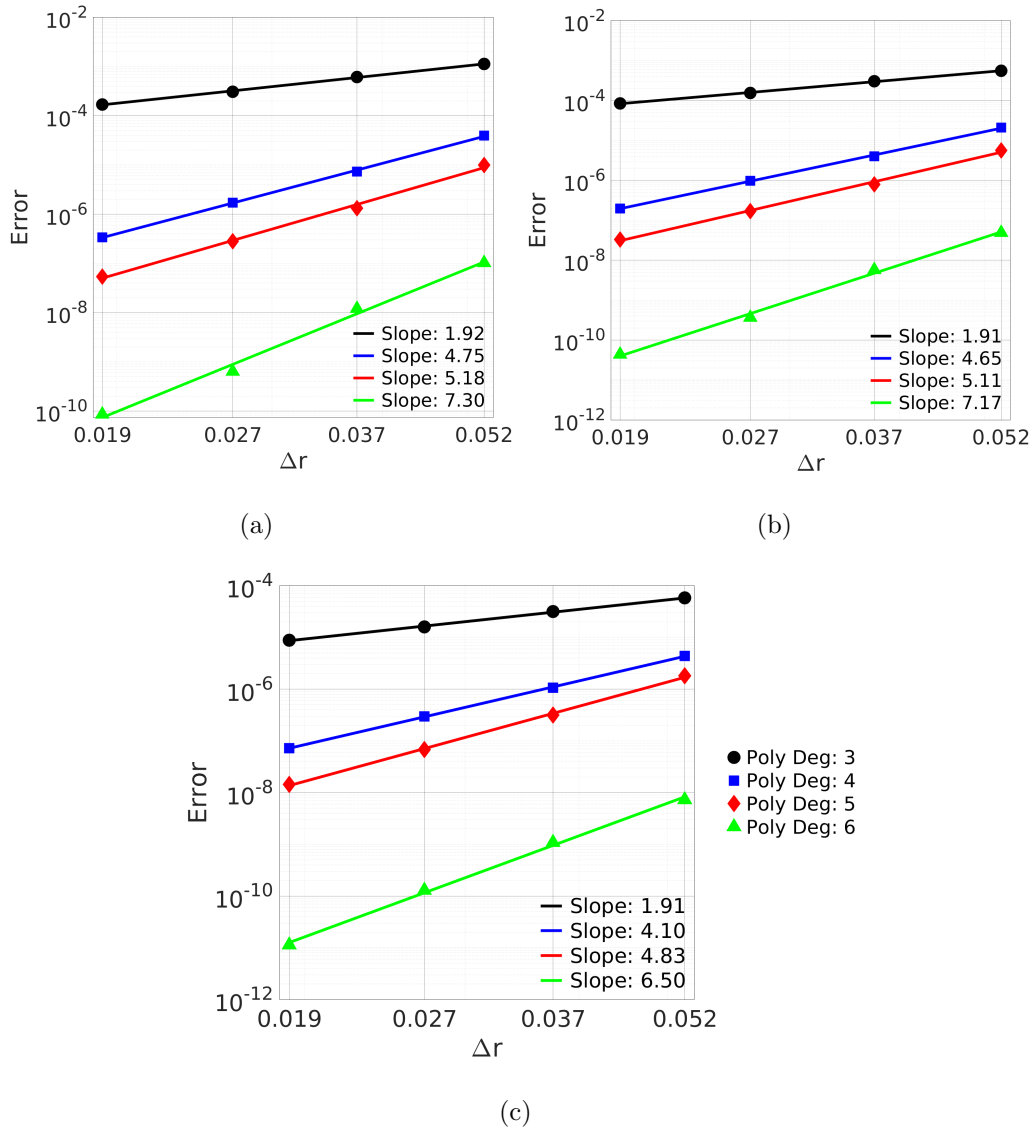


Figure 14: Circle inside a square: Average error vs. Δr in the entire domain for thermal conductivity ratios: (a) 5, (b) 10 and (c) 100.

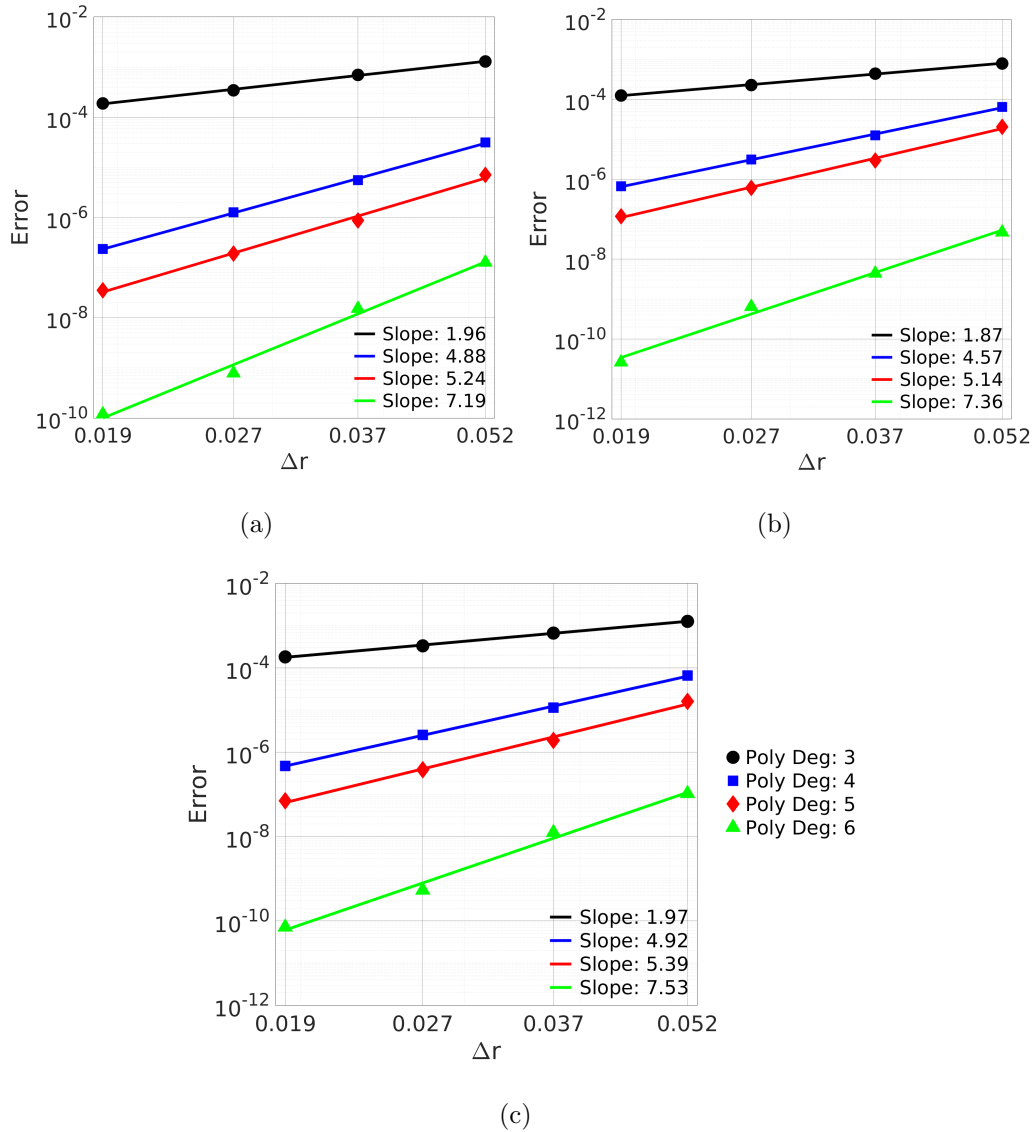


Figure 15: Circle inside a square: Average error vs. Δr in subdomains for thermal conductivity ratio of 10: (a) domain I, (b) domain II and (c) interface.

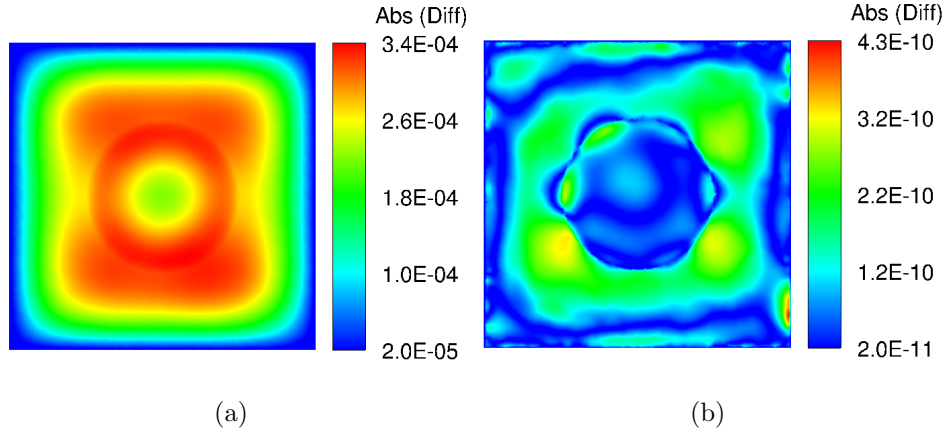


Figure 16: Circle inside a square: Contours of absolute differences between computed and exact solutions for thermal conductivity ratio of 10 and with 12078 scattered points: (a) polynomial degree = 3 and (b) polynomial degree = 6.

4.2. Astroidal domain inside a square

The second problem considered for accuracy assessment is a geometry with sharp corners. Modelling interfaces with sharp corners remains a challenge as most of the traditional CFD techniques such as finite difference (FDM), finite volume (FVM), boundary element (BEM) methods, etc may require high grid resolution to give accurate results. To test the applicability of PHS-RBF for such problems, we have considered a 2D astroidal shaped domain inside a square section. Figure 17 shows the positions of 540 points within the domain.

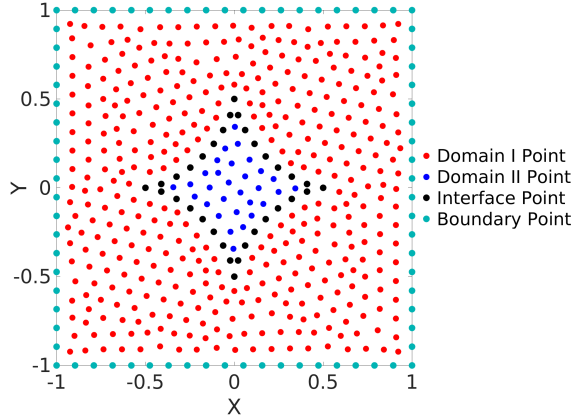


Figure 17: Astroidal domain inside a square: Locations of 540 points within the domain.

The external boundary points are represented by cyan coloured dots and are part of domain I. The parametric equation for the interface is given by

$$\begin{aligned} x &= a \cos^3 \theta & 0 \leq \theta \leq 2\pi; \quad a = 0.5 \\ y &= a \sin^3 \theta \end{aligned} \quad (16)$$

The manufactured temperature distribution given by eq. (17) satisfies the flux conditions at the interface. A surface plot of the distribution is shown in fig. 18 for thermal conductivity ratio of 10 i.e. $k_I = 10$ and $k_{II} = 1$.

$$\begin{aligned} T_I &= k_{II} \sin \left(x^4 y^4 \left(\left(\frac{x}{a} \right)^{\frac{2}{3}} + \left(\frac{y}{a} \right)^{\frac{2}{3}} - 1 \right) \right) \\ T_{II} &= k_I \sin \left(x^4 y^4 \left(\left(\frac{x}{a} \right)^{\frac{2}{3}} + \left(\frac{y}{a} \right)^{\frac{2}{3}} - 1 \right) \right) \end{aligned} \quad (17)$$

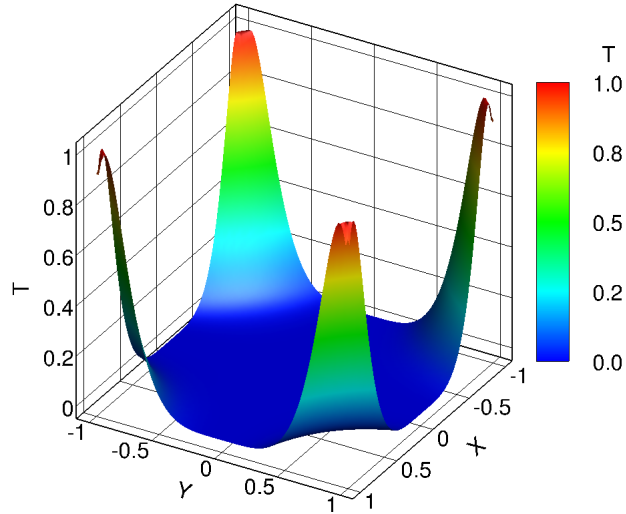


Figure 18: Astroidal domain inside a square: Surface plot of the manufactured temperature distribution for the astroidal geometry inside a square.

Figure 19 plots the variation of the average absolute difference between the computed and the exact temperatures as a function of the average point spacing for four different distribution of data points within each subdomain (Table 2). Figures 19(a) to 19(c) are for conductivity ratios of 5, 10 and 100. It can be noted from fig. 19 that error decreases as expected with the degree of the appended polynomial, even for the conductivity ratio of 100. The conductivity ratio does not appear to influence the accuracy. This observation is very encouraging compared to a single domain method which tends to smear the sharp discontinuity and produce erroneous results.

Δr	N	N_I	N_{II}	N_{Int}
0.053	1523	1396	79	48
0.038	3038	2769	197	72
0.027	6084	5568	412	104
0.019	12060	11080	832	148

Table 2: Astroidal domain inside a square: Average grid spacing (Δr) with the corresponding total number of points distributed within the entire domain (N) and subdomains i.e. Domain I (N_I), Domain II (N_{II}) and Interface (N_{Int}).

In fig. 20, we plot the averaged error only for the interface points. As stated earlier, the governing equation is not satisfied at the interface points. Only the flux is ensured to be continuous. Hence the interface is prone to larger errors than the domains where the governing equation is satisfied. However, we observe that even for the interface points, taken in isolation, the error is small and decreases as expected with the degree of the appended polynomial. The same conclusion can be drawn from the error contours ($\text{Abs}(\text{Diff}) = |T_{exact} - T_{calc}|$) shown in fig. 21 with 12060 scattered points for polynomial degrees 3 and 6. Interestingly, the errors are largest near the four corners of the external boundary and not at the interface.

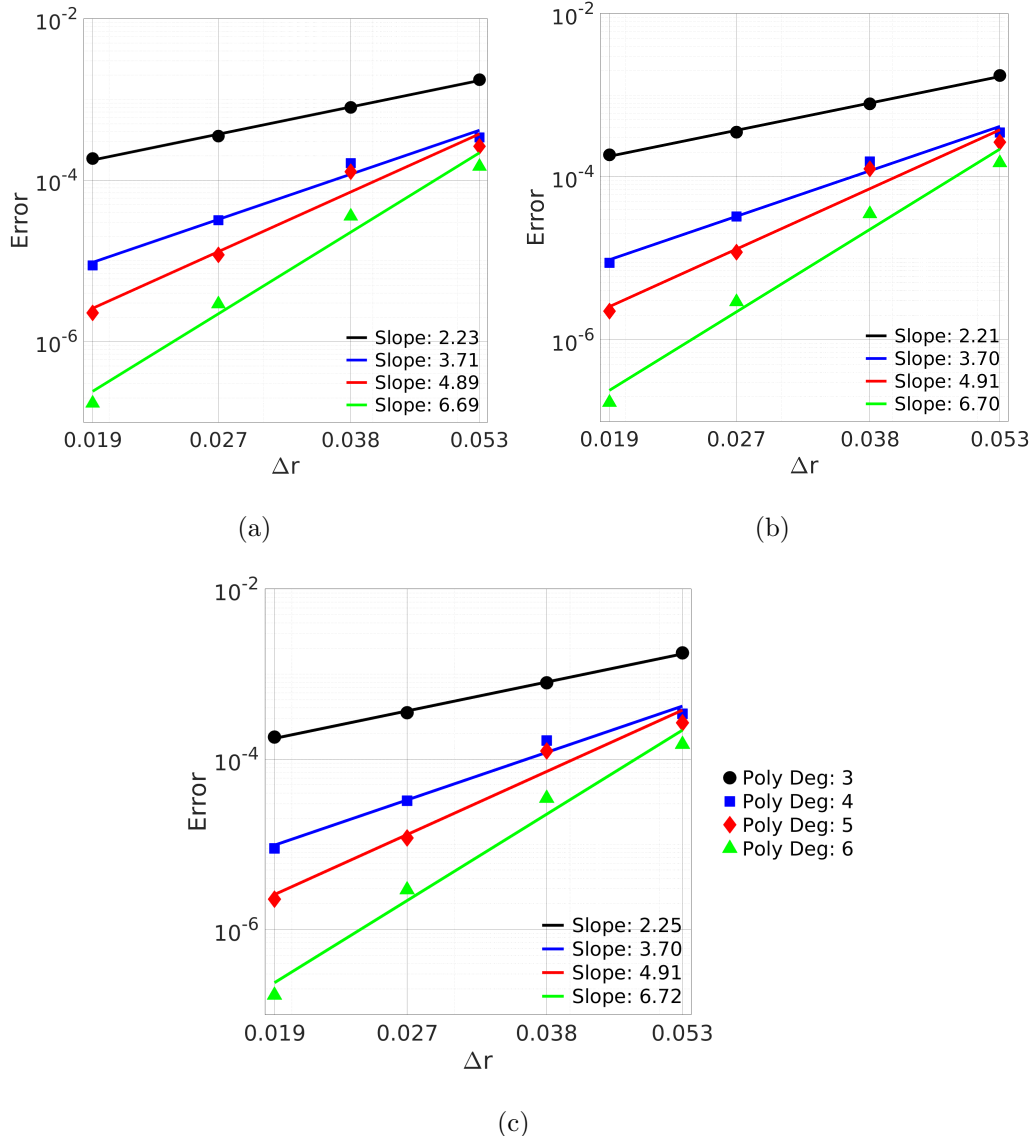


Figure 19: Astroidal domain inside a square: Average error vs. Δr in the entire domain for thermal conductivity ratios: (a) 5, (b) 10 and (c) 100.

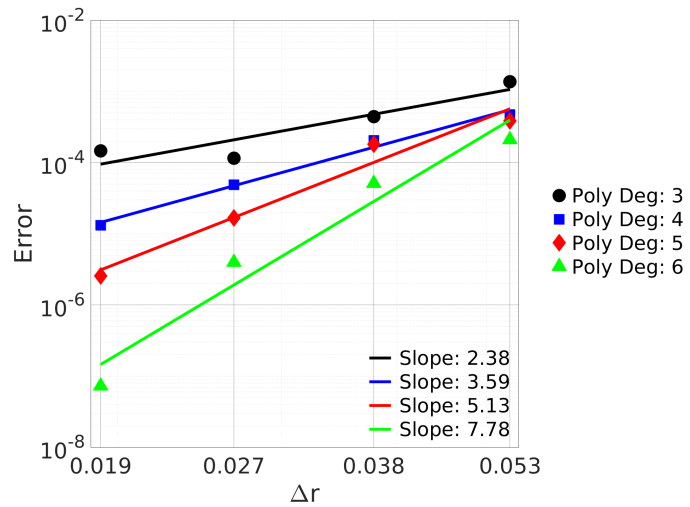


Figure 20: Astroidal domain inside a square: Variation of error at interface points for conductivity ratio of 10.

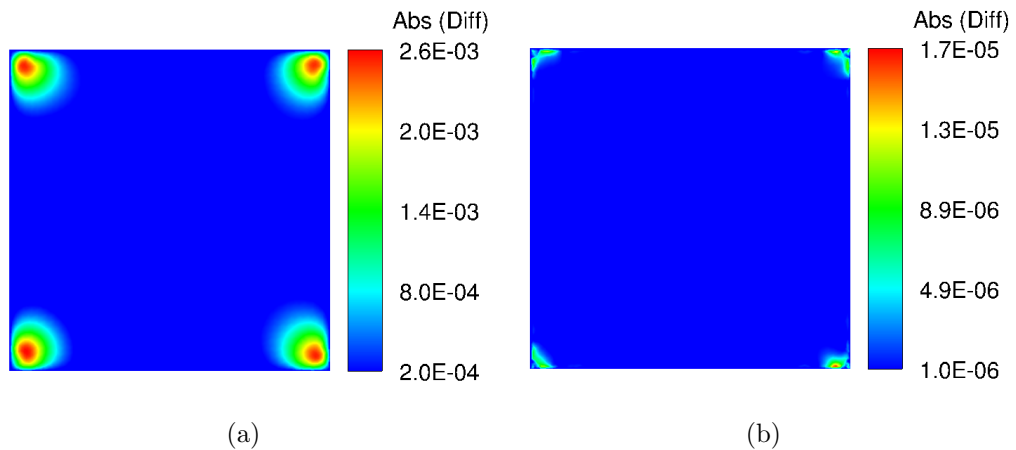


Figure 21: Astroidal domain inside a square: Contours of absolute differences between computed and exact solutions for thermal conductivity ratio of 10 and with 12060 scattered points: (a) polynomial degree = 3 and (b) polynomial degree = 6.

4.3. Sphere inside a cube

We next consider a three-dimensional problem of a sphere inside a cube. The sphere is of radius 0.5 units and the cube is 2 units on its side. The solution domain consists of three sets of points. Domain I is the region between the surface of the sphere and inside the cube. Domain II is the set of points inside the sphere. The interface is separately discretized by its own scattered points. Figure 22 shows the layout of the scattered points.

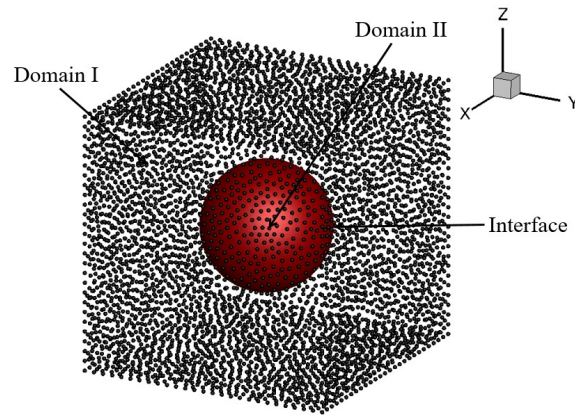


Figure 22: Sphere inside a cube: Illustrative point layout for sphere inside a cube.

A manufactured temperature distribution given by eq. (18) and illustrated in fig. 23 for conductivity ratio of 10 is used for accuracy estimation.

$$\begin{aligned} T_I &= k_{II} \sin(x^2 + y^2 + z^2 - r^2) \\ T_{II} &= k_I \sin(x^2 + y^2 + z^2 - r^2) \end{aligned} \tag{18}$$

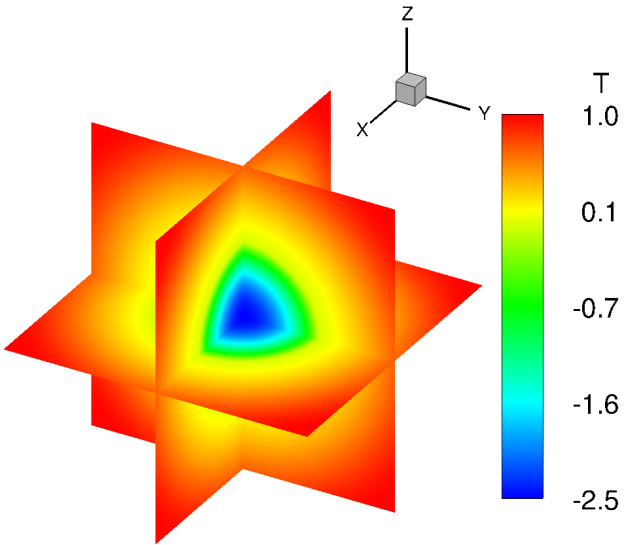


Figure 23: Sphere inside a cube: 3D view of the manufactured temperature distribution.

Four sets of scattered points consisting of 28961, 87680, 299798 and 711041 total points with average spacing of 0.057, 0.04, 0.026 and 0.018 units are considered for polynomial degree from 3 to 6. The number of points in different regions is given in table 3.

Δr	N	N_I	N_{II}	N_{Int}
0.057	28961	14466	10326	4169
0.040	87680	50610	28826	8244
0.026	299798	170789	107603	21406
0.018	711041	379939	293838	37264

Table 3: Sphere inside a cube: Average grid spacing (Δr) with the corresponding total number of points distributed within the entire domain (N) and subdomains i.e. Domain I (N_I), Domain II (N_{II}) and Interface (N_{Int}).

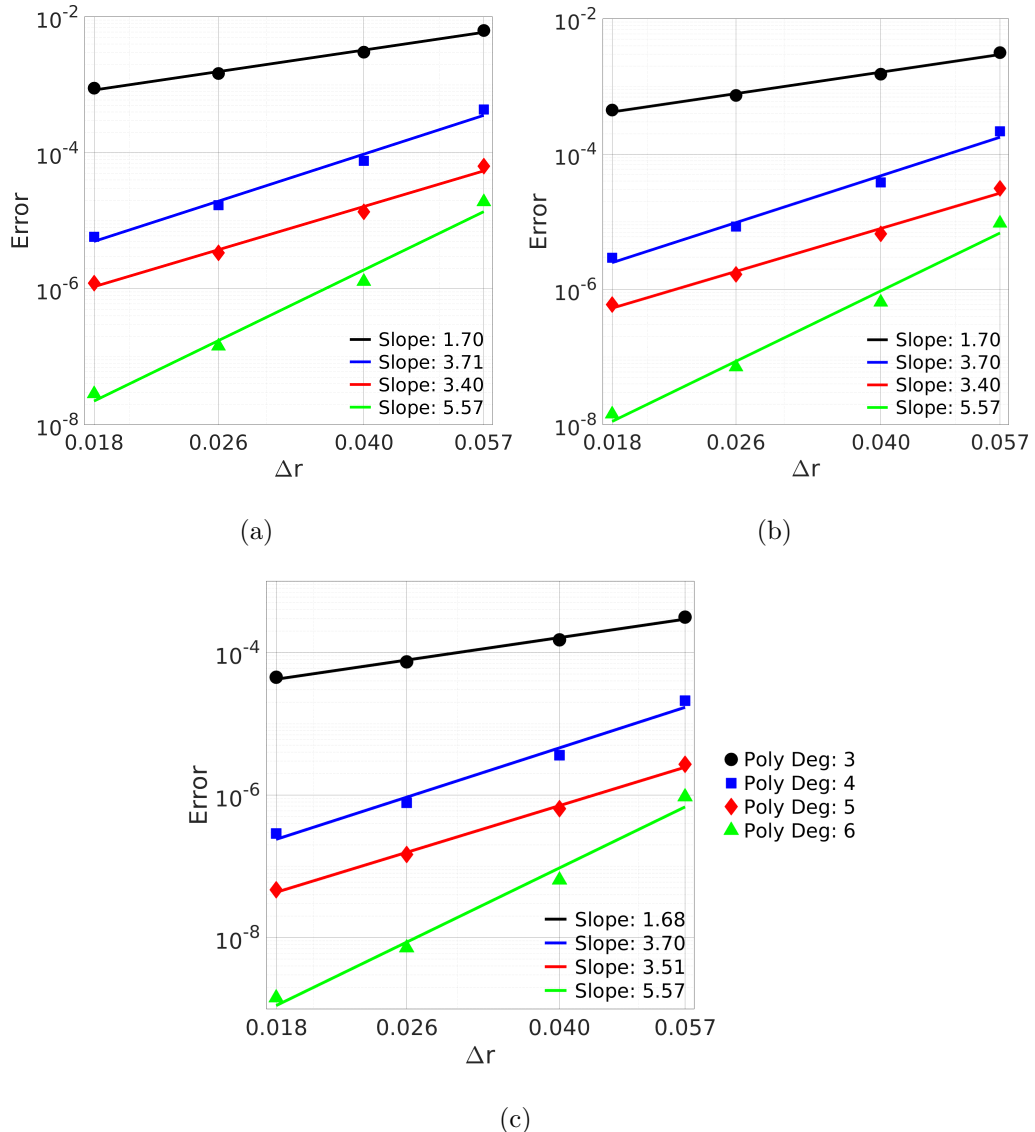


Figure 24: Sphere inside a cube: Average error vs. Δr in the entire domain for thermal conductivity ratios: (a) 5, (b) 10 and (c) 100.

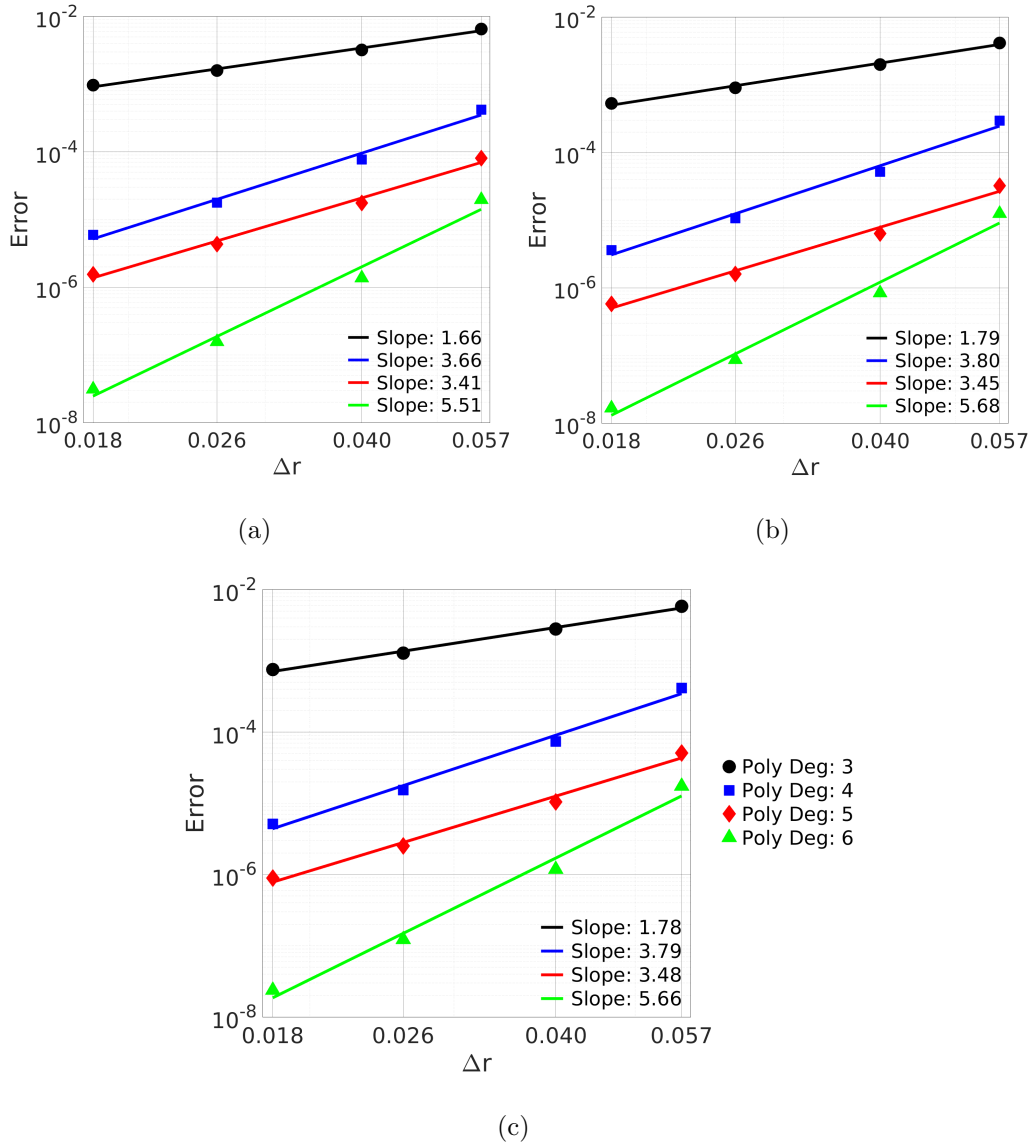


Figure 25: Sphere inside a cube: Average error vs. Δr in subdomains for thermal conductivity ratio of 10: (a) domain I, (b) domain II and (c) interface.

Figure 24 shows the variation of the discretization error with the average grid spacing for thermal conductivity ratios of 5, 10 and 100. In Figure 25, we show the variation for the three subdomains separately for thermal conductivity ratio of 10. We demonstrate that the expected error reduction is also achieved in the three dimensional problems. It can be noted from fig. 25(c) that at the interface, the order of convergence increases from 1.78 at polynomial degree of 3 to 5.66 at polynomial degree of 6. Figure 26 presents the difference between numerically computed and manufactured temperature on three orthogonal planes at $X = 0$, $Y = 0$ and $Z = 0$ for two polynomial degrees 3 and 6 with 711041 points. The conductivity ratio is 10.

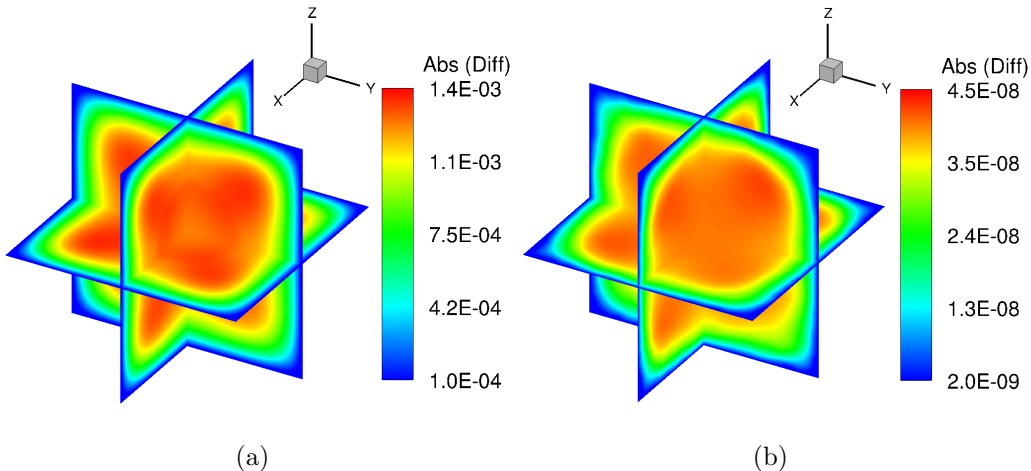


Figure 26: Sphere inside a cube: Contours of absolute differences between computed and exact solutions for thermal conductivity ratio of 10 and with 711041 scattered points: (a) polynomial degree = 3 and (b) polynomial degree = 6.

4.4. Convergence plots

A comprehensive analysis of the order of convergence (C) with the degree of appended polynomial (p) for the three problems discussed in sections 4.1 to 4.3 is presented in figs. 27 to 30 for thermal conductivity ratio of 10 and 100. The composite plot of the error is presented individually for each subdomain and the interface, followed by the error for the entire domain. Results are presented for all the polynomials in the same plot. Two lines $C = p - 1$ (green line) and $C = p + 1$ (red line) are also drawn where p is the degree of the appended polynomial. It is observed that the order of convergence lies almost within the regions bounded by $C = p - 1$ and $C = p + 1$ corresponding to a specified degree of appended polynomial. In the current study, the most critical subdomain is the interface. It can be noted from fig. 29 that even at the interface, the error decreases with the increase in the degree of the polynomial.

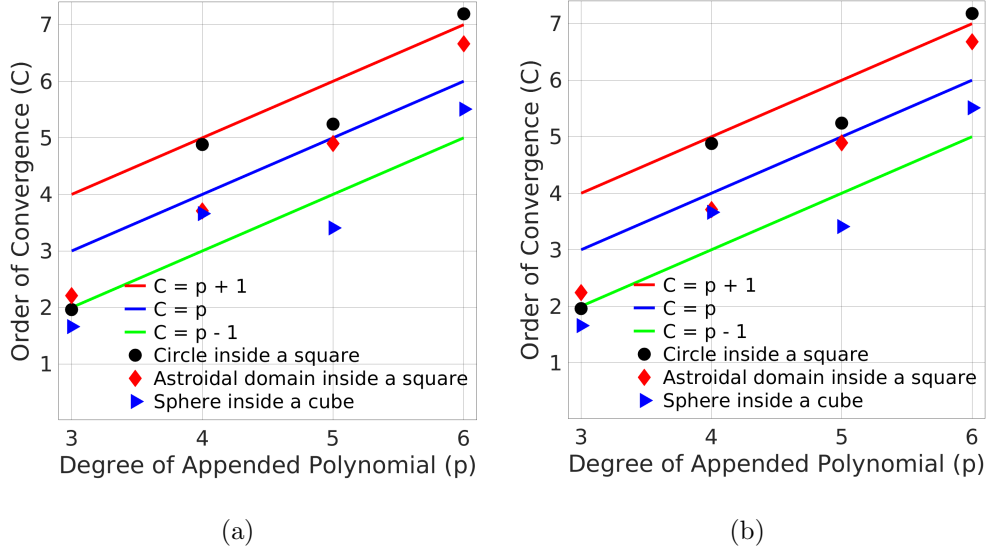


Figure 27: Convergence plots: Order of convergence (C) vs. Degree of appended polynomial (p) for domain I with thermal conductivity ratios of (a) 10 and (b) 100.

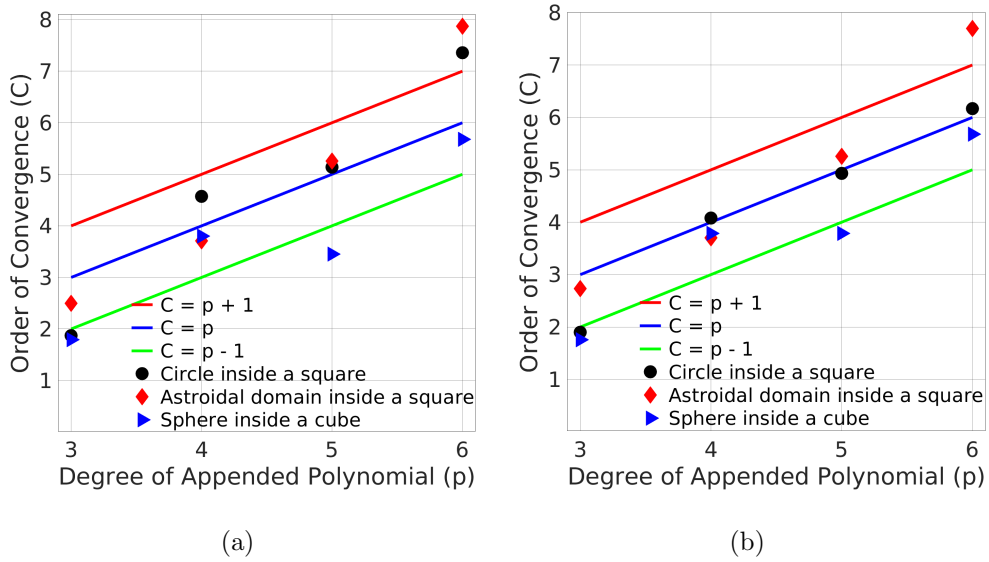


Figure 28: Convergence plots: Order of convergence (C) vs. Degree of appended polynomial (p) for domain II with thermal conductivity ratios of (a) 10 and (b) 100.

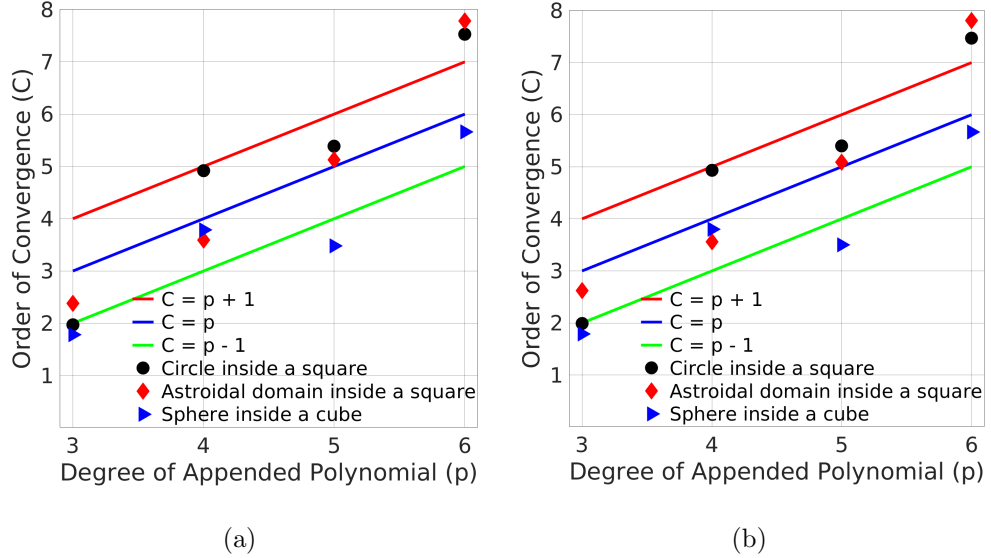


Figure 29: Convergence plots: Order of convergence (C) vs. Degree of appended polynomial (p) for interface with thermal conductivity ratios of (a) 10 and (b) 100.

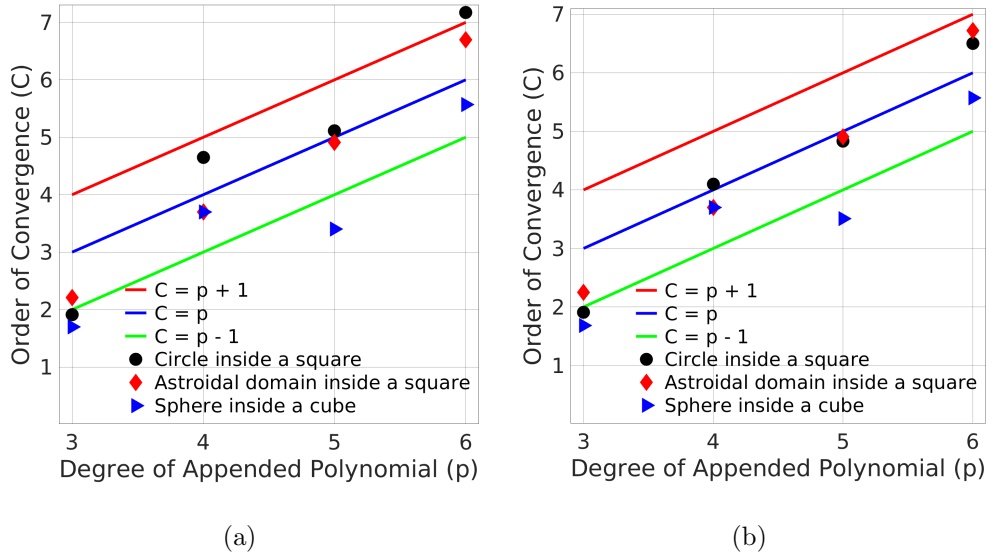


Figure 30: Convergence plots: Order of convergence (C) vs. Degree of appended polynomial (p) for the entire domain with thermal conductivity ratios of (a) 10 and (b) 100.

5. Application to complex problems

In this section, we demonstrate the applicability of the multidomain meshless algorithm to complex geometries in two and three dimensions with realistic boundary conditions instead of manufactured solutions. First, we study a couple of two dimensional domains: (i) astroidal domain inside a square and (ii) multiple circular and elliptical subdomains within a square section. Grid independence tests are also performed for the given geometries. Later, a couple of three dimensional geometries: (i) wavy circular tube inside a straight circular tube and (ii) multiple cylindrical fillets inside a cube are simulated to demonstrate the robustness of PHS-RBF algorithm.

5.1. Astroidal domain inside a square

We have modified the two dimensional case presented earlier (section 4.2) by imposing $T = 0$ at the outer boundary and prescribing a heat generation rate of 100 units inside the astroidal domain. The conductivity ratio is set to either 2 or 100. The temperature distribution for both the cases are shown in fig. 31. It can be seen that for the first case (fig. 31(a)) that there is a relatively large diffusion of heat as compared to the second case (fig. 31(b)) where the thermal conductivity in domain I is higher i.e. $k_I = 100$, hence the temperature gradient is lower. Therefore, the second case shows a sharper jump in temperature across the interface.

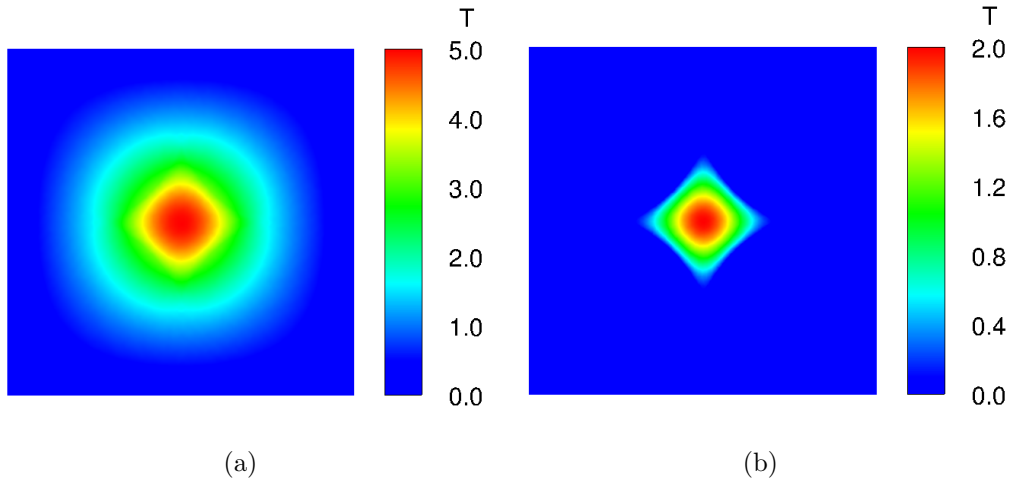


Figure 31: Astroidal domain inside a square: Temperature contours: (a) $\frac{k_I}{k_{II}} = 2$ and (b) $\frac{k_I}{k_{II}} = 100$.

Grid independence tests are also performed for both the cases as shown in figs. 32(a) and 32(b) for the degree of appended polynomial of 6. The temperature variations along a diagonal of the square are plotted for the two conductivity ratios using up to a total of 6084 scattered points. As the horizontal (X) and vertical coordinates (Y) of the points along the diagonal are the same, the variation of temperature (T) is shown with respect to the horizontal distance (X) from the bottom left corner of the square.

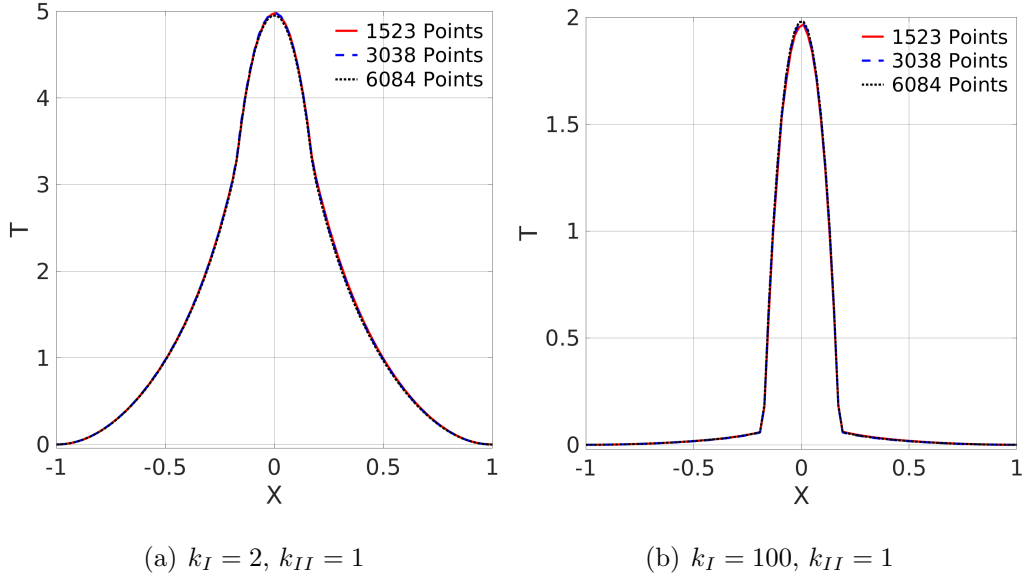


Figure 32: Astroidal domain inside a square: Grid independence test for an astroidal domain inside a square.

Table 4 presents the average temperatures in the solution domain for conductivity ratios of 2 and 100 at polynomial degree of 6. Similar results are seen for polynomial degrees from 3 to 5.

Points	Average temperature for case (a)	Average temperature for case (b)
1523	0.966	0.071
3038	1.015	0.078
6084	1.011	0.079

Table 4: Astroidal domain inside a square: Average temperatures over the domain for case (a) and case (b).

5.2. A square with embedded circular and elliptical domains

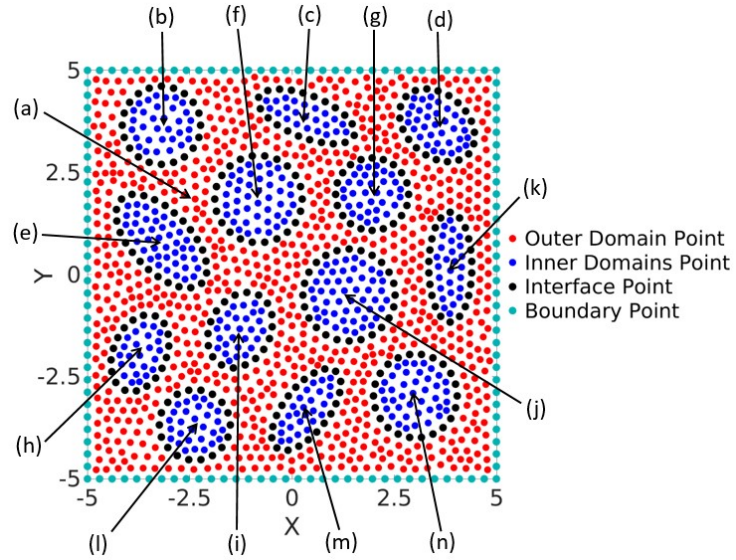


Figure 33: A square with embedded circular and elliptical domains: Layout of 1574 scattered points.

We next consider a complex domain consisting of circular and elliptical subdomains embedded within a square. A square with a side of 10 units encloses 13 circular and elliptical subdomains of different sizes and aspect ratios. The geometry emulates composite materials having varying thermo-physical characteristics. Figure 33 shows the layout of 1574 points within the domain divided into multiple subdomains. The outer region is marked by red dots and the different subdomains resolving the ellipses and circles are discretized by the blue coloured points. Black dots represent the interfaces of different subdomains with the outer domain.

Within each subdomain, there is either a heat source or sink as tabulated in table 5. The external boundary is maintained at a temperature $T = 0$.

Table 5 also lists the total number of scattered points distributed within each subdomain and on the corresponding interface. The total number of points in the entire domain is 15032.

Subdomain	k	\dot{q}	No. of points	No. of points on the interface or boundary
a	100	0	8954	444
b	1	100	408	68
c	3	-300	270	64
d	5	500	349	64
e	1	-100	453	78
f	3	300	482	74
g	5	-500	334	62
h	1	100	279	58
i	3	-300	312	60
j	5	500	541	78
k	1	-100	292	68
l	3	300	316	60
m	5	-500	273	62
n	1	100	457	72

Table 5: A square with embedded circular and elliptical domains: Thermal conductivity (k), rate of heat generation (\dot{q}), number of interior points and interface points for the various domains.

Figure 34 shows the temperature contours for the given boundary and interior conditions for a polynomial degree of 6. Due to the high thermal conductivity prescribed in the outer domain, the temperature gradients in this region are relatively small. The temperature distributions in the interior subdomains are according to the heat generation prescribed. The contours of temperature display expected qualitative trends.

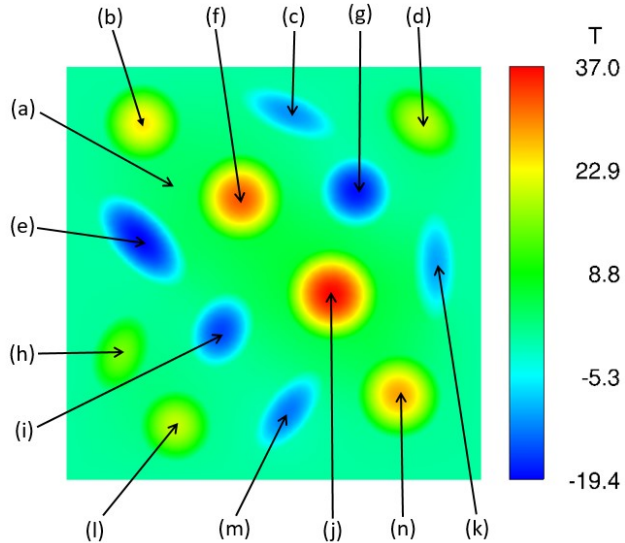


Figure 34: A square with embedded circular and elliptical domains: Temperature contours in a square with heat generating elliptical and circular subdomains.

Grid independency tests are also performed with four different point layouts consisting of 5065, 10015, 15032 and 20016 points for the degree of appended polynomial of 6. Figure 35 shows the temperature variation on the diagonals from $(-5, -5)$ to $(5, 5)$ and $(-5, 5)$ to $(5, -5)$. The variation is shown with respect to the X coordinates of the points along the diagonals. It can be seen that the temperature distributions overlap for the different

point sets, implying fast convergence of the solutions. Table 6 gives the convergence of the average temperatures over the entire domain.

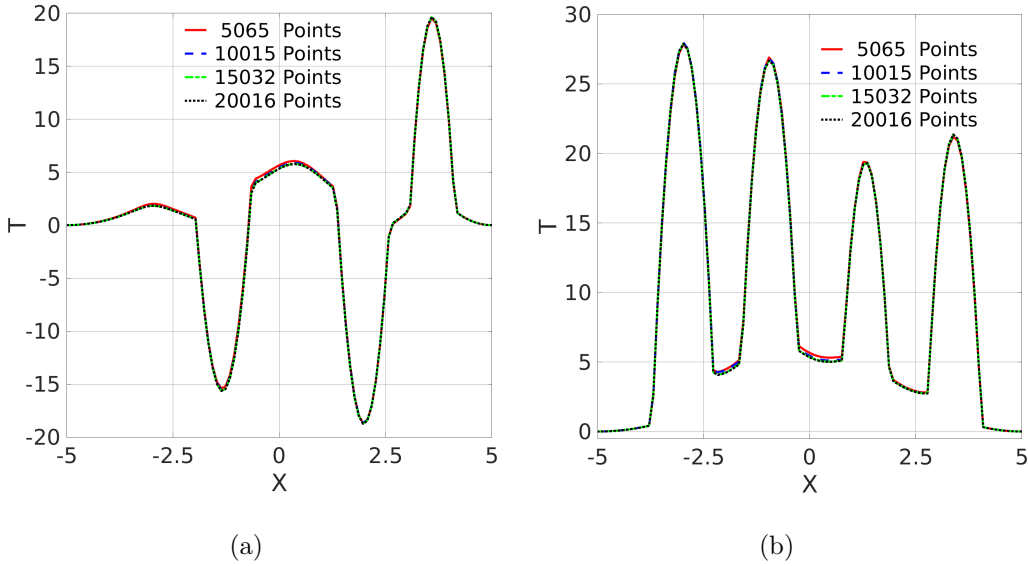


Figure 35: A square with embedded circular and elliptical domains: Temperature profiles along the two cross-diagonals for different point distributions.

Number of points	Average temperature
5065	2.587
10015	2.744
15032	2.706
20016	2.706

Table 6: A square with embedded circular and elliptical domains: Average temperatures for different point sets.

5.3. Wavy circular tube inside a straight circular tube

We next consider two three-dimensional geometries to demonstrate the applicability of the method to complex three-dimensional problems. Figure 36 shows a wavy circular tube of radius 0.4 unit and length of 5 units confined in a straight circular tube of radius 1 unit and length of 6 units. The region outside the wavy circular tube is marked as domain I, the region within the wavy tube is marked as domain II, and the surface of the tube is marked as the interface. The wavy circular tube has an internal heat generation rate of 100 units.

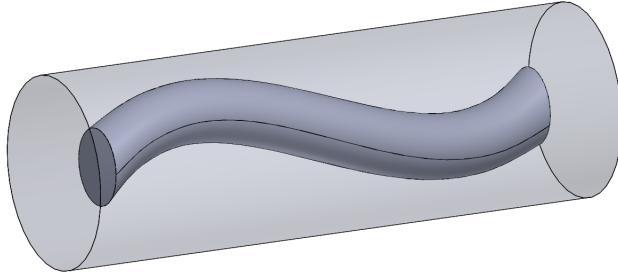


Figure 36: Wavy circular tube inside a straight circular tube.

Two test cases with diffusion coefficient ratios of $\frac{k_I}{k_{II}} = 2$ and 100 are considered. Figure 37 shows the temperature contours for both the cases at five planes orthogonal to Z axis i.e. at $Z = 1, 2, 3, 4$ and 5 units with 100220 scattered points distributed throughout the domain. The temperature contours are more diffused in fig. 37(a) as compared to fig. 37(b) due to lower thermal conductivity ratio $\left(\frac{k_I}{k_{II}}\right)$, hence relatively higher values of temperature gradient in domain I. Figure 38 shows the isosurfaces of temperature for both the cases.

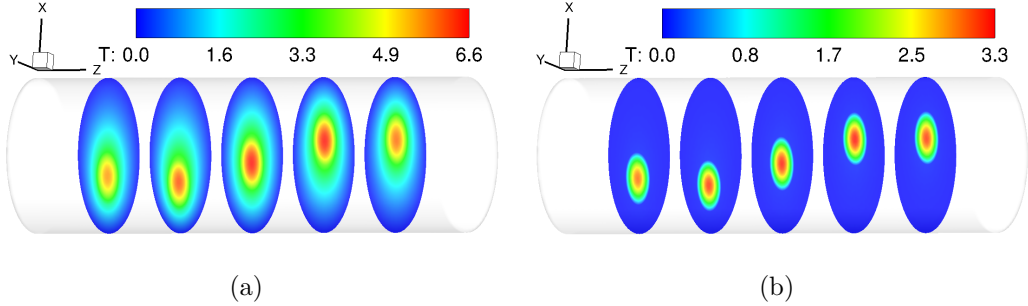


Figure 37: Wavy circular tube inside a straight circular tube: Temperature contours: (a) $\frac{k_L}{k_{II}} = 2$ and (b) $\frac{k_L}{k_{II}} = 100$.



Figure 38: Wavy circular tube inside a straight circular tube: Isosurfaces: (a) $\frac{k_L}{k_{II}} = 2$ and (b) $\frac{k_L}{k_{II}} = 100$.

5.4. A complex dispersion of cylindrical fillets inside a cube

The last three dimensional problem consists of 16 cylindrical fillets of radius = 0.3 unit, length = 1.73 units within a cube of dimensions 6 units \times 6 units \times 6 units as shown in fig. 39. The cylindrical fillets are arranged in such a way that adequate space exists between the fillets to place sufficient number of points.

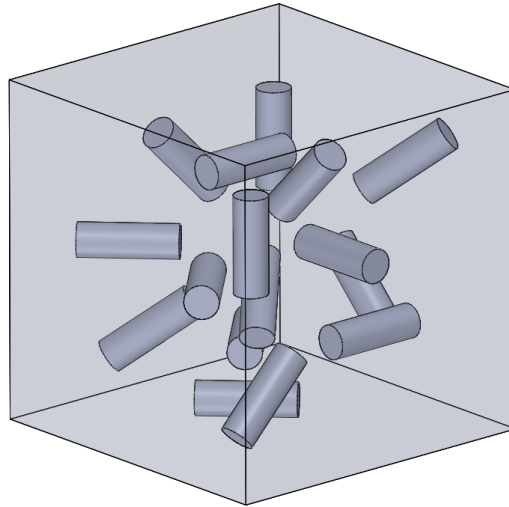


Figure 39: Geometry for multiple cylindrical fillets inside a cube.

The cylindrical fillets are assigned to be either a heat source or a heat sink with different thermal conductivities. The values of the diffusion coefficients have been assigned to be higher in the non-fillet regions than inside the fillets. A total of 198545 points are used to discretize the three-dimensional region using vertices of a finite element grid. A polynomial degree of 6 is used for the PHS-RBF. The outer boundary is assigned a temperature of zero on all six faces. A steady state temperature distribution is computed and the isosurfaces of the same is shown in fig. 40.

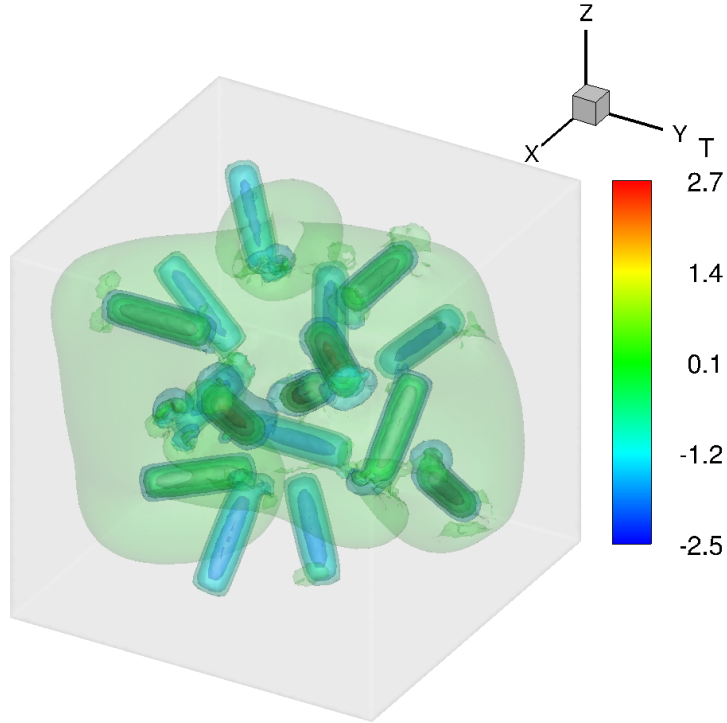


Figure 40: A complex dispersion of cylindrical fillets inside a cube: Three-dimensional distributions of temperature for the fillet geometry.

6. Summary and Future work

In this paper, we have described a multidomain cloud based numerical algorithm for computing heat transfer in complex domains with significant variations of thermo-physical properties. The algorithm interpolates variables at scattered points using polyharmonic splines and appended polynomial. At the interfaces between subdomains, the fluxes are balanced, and the clouds of interpolation points are restricted to be within individual subdomains. We show that the imposition of the flux balance condition at the interface points (and not satisfying the governing equation) does not de-

grade the expected high accuracy of the overall algorithm. Several two and three-dimensional simulations with manufactured solutions have been performed for different conductivity ratios, degree of the appended polynomial and inter-point spacings. The expected high accuracy is observed for all the problems. Further, a couple of two and three dimensional problems in complex domains are simulated to demonstrate the capability of the algorithm. The proposed multidomain algorithm has the potential to study fluid flow and convective heat transfer in complex domains, including natural convection, phase change and multiphysics phenomena such as coupling with electromagnetics, radiative heat transfer, etc. These will be considered in the future.

Acknowledgement

Naman Bartwal would like to thank his labmate Siddharth D. Sharma for fruitful discussions on modeling of geometries. The authors acknowledge SPARC (Scheme for Promotion of Academic and Research Collaboration → Project code: P1211) for its financial support.

Declaration of Interests

The authors declare that they have no known competing financial interests or personal relationships that could have appeared to influence the work reported in this paper.

References

References

- [1] H. M. Ali, M. M. Janjua, U. Sajjad, W. M. Yan, et al., A critical review on heat transfer augmentation of phase change materials embedded with porous materials/foams, *International Journal of Heat and Mass Transfer* 135 (2019) 649–673.
- [2] M. Aramesh, B. Shabani, Metal foams application to enhance the thermal performance of phase change materials: A review of experimental studies to understand the mechanisms, *Journal of Energy Storage* 50 (2022) 104650.
- [3] A. Bhowmik, R. Singh, R. Repaka, S. C. Mishra, Conventional and newly developed bioheat transport models in vascularized tissues: A review, *Journal of Thermal biology* 38 (2013) 107–125.
- [4] Q. Wang, Y. X. Ren, W. Li, Compact high order finite volume method on unstructured grids i: Basic formulations and one-dimensional schemes, *Journal of Computational Physics* 314 (2016) 863–882.
- [5] Q. Wang, Y. X. Ren, W. Li, Compact high order finite volume method on unstructured grids ii: Extension to two-dimensional euler equations, *Journal of Computational Physics* 314 (2016) 883–908.
- [6] Y. Liu, W. Zhang, Y. Jiang, Z. Ye, A high-order finite volume method on unstructured grids using rbf reconstruction, *Computers & Mathematics with Applications* 72 (2016) 1096–1117.

- [7] S. Shahane, A. Radhakrishnan, S. P. Vanka, A high-order accurate meshless method for solution of incompressible fluid flow problems, *Journal of Computational Physics* 445 (2021) 110623.
- [8] S. Shahane, S. P. Vanka, A semi-implicit meshless method for incompressible flows in complex geometries, *arXiv preprint arXiv:2106.07616* (2021).
- [9] N. Bartwal, S. Shahane, S. Roy, S. P. Vanka, Application of a high order accurate meshless method to solution of heat conduction in complex geometries, *Computational Thermal Sciences: An International Journal* 14 (2022).
- [10] S. Shahane, S. P. Vanka, Consistency and convergence of a high order accurate meshless method for solution of incompressible fluid flows, *arXiv preprint arXiv:2202.02828* (2022).
- [11] A. Unnikrishnan, S. Shahane, V. Narayanan, S. P. Vanka, Shear-driven flow in an elliptical enclosure generated by an inner rotating circular cylinder, *Physics of Fluids* 34 (2022) 013607.
- [12] E. J. Kansa, Multiquadratics - A scattered data approximation scheme with applications to computational fluid-dynamics - I, surface approximations and partial derivative estimates, *Computers & Mathematics with applications* 19 (1990) 127–145.
- [13] E. J. Kansa, Multiquadratics - A scattered data approximation scheme with applications to computational fluid-dynamics - II, solutions to

parabolic, hyperbolic and elliptic partial differential equations, Computers & mathematics with applications 19 (1990) 147–161.

- [14] R. L. Hardy, Multiquadric equations of topography and other irregular surfaces, Journal of geophysical research 76 (1971) 1905–1915.
- [15] A. Mayo, The fast solution of poisson's and the biharmonic equations on irregular regions, SIAM Journal on Numerical Analysis 21 (1984) 285–299.
- [16] A. Mayo, Fast high order accurate solution of laplace's equation on irregular regions, SIAM journal on scientific and statistical computing 6 (1985) 144–157.
- [17] R. J. LeVeque, Z. Li, The immersed interface method for elliptic equations with discontinuous coefficients and singular sources, SIAM Journal on Numerical Analysis 31 (1994) 1019–1044.
- [18] Z. Chen, J. Zou, Finite element methods and their convergence for elliptic and parabolic interface problems, Numerische Mathematik 79 (1998) 175–202.
- [19] Z. Li, Y. Q. Shen, A numerical method for solving heat equations involving interfaces, in: Electronic Journal of Differential Equations, Conf, volume 3, 1999, pp. 100–108.
- [20] X. D. Liu, R. P. Fedkiw, M. Kang, A boundary condition capturing method for poisson's equation on irregular domains, Journal of computational Physics 160 (2000) 151–178.

- [21] F. Gibou, R. P. Fedkiw, L.-T. Cheng, M. Kang, A second-order-accurate symmetric discretization of the poisson equation on irregular domains, *Journal of Computational Physics* 176 (2002) 205–227.
- [22] Z. Li, T. Lin, X. Wu, New cartesian grid methods for interface problems using the finite element formulation, *Numerische Mathematik* 96 (2003) 61–98.
- [23] S. Hou, X. D. Liu, A numerical method for solving variable coefficient elliptic equation with interfaces, *Journal of Computational Physics* 202 (2005) 411–445.
- [24] C. Shu, H. Ding, K. Yeo, Local radial basis function-based differential quadrature method and its application to solve two-dimensional incompressible navier–stokes equations, *Computer methods in applied mechanics and engineering* 192 (2003) 941–954.
- [25] E. Larsson, B. Fornberg, A numerical study of some radial basis function based solution methods for elliptic pdes, *Computers & Mathematics with Applications* 46 (2003) 891–902.
- [26] H. Ding, C. Shu, K. Yeo, D. Xu, Numerical computation of three-dimensional incompressible viscous flows in the primitive variable form by local multiquadric differential quadrature method, *Computer Methods in Applied Mechanics and Engineering* 195 (2006) 516–533.
- [27] Y. Sanyasiraju, G. Chandhini, Local radial basis function based gridfree scheme for unsteady incompressible viscous flows, *Journal of Computational Physics* 227 (2008) 8922–8948.

- [28] G. Chandhini, Y. Sanyasiraju, Local rbf-fd solutions for steady convection–diffusion problems, *International Journal for Numerical Methods in Engineering* 72 (2007) 352–378.
- [29] Y. Sanyasiraju, G. Chandhini, A note on two upwind strategies for rbf-based grid-free schemes to solve steady convection–diffusion equations, *International journal for numerical methods in fluids* 61 (2009) 1053–1062.
- [30] A. Vidal, A. J. Kassab, E. A. Divo, A direct velocity-pressure coupling meshless algorithm for incompressible fluid flow simulations, *Engineering Analysis with Boundary Elements* 72 (2016) 1–10.
- [31] R. Zamolo, E. Nobile, Solution of incompressible fluid flow problems with heat transfer by means of an efficient rbf-fd meshless approach, *Numerical Heat Transfer, Part B: Fundamentals* 75 (2019) 19–42.
- [32] J. C. Mairhuber, On haar’s theorem concerning chebychev approximation problems having unique solutions, *Proceedings of the American Mathematical Society* 7 (1956) 609–615.
- [33] M. Buhmann, N. Dyn, Spectral convergence of multiquadric interpolation, *Proceedings of the Edinburgh Mathematical Society* 36 (1993) 319–333.
- [34] S. Wong, Y. Hon, M. A. Golberg, Compactly supported radial basis functions for shallow water equations, *Applied mathematics and computation* 127 (2002) 79–101.

- [35] B. Fornberg, G. Wright, Stable computation of multiquadric interpolants for all values of the shape parameter, *Computers & Mathematics with Applications* 48 (2004) 853–867.
- [36] B. Fornberg, G. Wright, E. Larsson, Some observations regarding interpolants in the limit of flat radial basis functions, *Computers & mathematics with applications* 47 (2004) 37–55.
- [37] E. Larsson, B. Fornberg, Theoretical and computational aspects of multivariate interpolation with increasingly flat radial basis functions, *Computers & Mathematics with Applications* 49 (2005) 103–130.
- [38] N. Flyer, G. B. Wright, A radial basis function method for the shallow water equations on a sphere, *Proceedings of the Royal Society A: Mathematical, Physical and Engineering Sciences* 465 (2009) 1949–1976.
- [39] B. Fornberg, E. Larsson, N. Flyer, Stable computations with gaussian radial basis functions, *SIAM Journal on Scientific Computing* 33 (2011) 869–892.
- [40] G. E. Fasshauer, M. J. McCourt, Stable evaluation of gaussian radial basis function interpolants, *SIAM Journal on Scientific Computing* 34 (2012) A737–A762.
- [41] B. Fornberg, E. Lehto, C. Powell, Stable calculation of gaussian-based rbf-fd stencils, *Computers & Mathematics with Applications* 65 (2013) 627–637.
- [42] N. Flyer, G. A. Barnett, L. J. Wicker, Enhancing finite differences

with radial basis functions: experiments on the navier–stokes equations, *Journal of Computational Physics* 316 (2016) 39–62.

- [43] G. A. Barnett, A robust RBF-FD formulation based on polyharmonic splines and polynomials, Ph.D. thesis, PhD thesis, University of Colorado Boulder, 2015.
- [44] N. Flyer, B. Fornberg, V. Bayona, G. A. Barnett, On the role of polynomials in rbf-fd approximations: I. interpolation and accuracy, *Journal of Computational Physics* 321 (2016) 21–38.
- [45] V. Bayona, N. Flyer, B. Fornberg, G. A. Barnett, On the role of polynomials in rbf-fd approximations: II. numerical solution of elliptic pdes, *Journal of Computational Physics* 332 (2017) 257–273.
- [46] L. Santos, N. Manzanares-Filho, G. Menon, E. Abreu, Comparing rbf-fd approximations based on stabilized gaussians and on polyharmonic splines with polynomials, *International Journal for Numerical Methods in Engineering* 115 (2018) 462–500.
- [47] V. Bayona, Comparison of moving least squares and rbf+ poly for interpolation and derivative approximation, *Journal of Scientific Computing* 81 (2019) 486–512.
- [48] V. Bayona, N. Flyer, B. Fornberg, On the role of polynomials in rbf-fd approximations: III. behavior near domain boundaries, *Journal of Computational Physics* 380 (2019) 378–399.
- [49] D. Miotti, R. Zamolo, E. Nobile, A fully meshless approach to the

numerical simulation of heat conduction problems over arbitrary 3d geometries, *Energies* 14 (2021) 1351.

- [50] A. Radhakrishnan, M. Xu, S. Shahane, S. P. Vanka, A non-nested multilevel method for meshless solution of the poisson equation in heat transfer and fluid flow, arXiv preprint arXiv:2104.13758 (2021).
- [51] T. Chu, O. T. Schmidt, Rbf-fd discretization of the navier-stokes equations using staggered nodes, arXiv preprint arXiv:2206.06495 (2022).
- [52] S. Reutskiy, A meshless radial basis function method for 2d steady-state heat conduction problems in anisotropic and inhomogeneous media, *Engineering Analysis with Boundary Elements* 66 (2016) 1–11.
- [53] M. Ahmad, E. Larsson, et al., Local meshless methods for second order elliptic interface problems with sharp corners, *Journal of Computational Physics* 416 (2020) 109500.
- [54] F. Gholampour, E. Hesameddini, A. Taleei, An efficient local rbf-based method for elasticity problems involving multiple material phases, *Engineering Analysis with Boundary Elements* 138 (2022) 189–201.
- [55] G. E. Karniadakis, S. Sherwin, *Spectral/hp element methods for computational fluid dynamics*, Oxford University Press on Demand, 2005.
- [56] C. Geuzaine, J. Remacle, Gmsh: A 3-d finite element mesh generator with built-in pre-and post-processing facilities, *International journal for numerical methods in engineering* 79 (2009) 1309–1331.

- [57] V. Shankar, R. M. Kirby, A. L. Fogelson, Robust node generation for mesh-free discretizations on irregular domains and surfaces, *SIAM Journal on Scientific Computing* 40 (2018) A2584–A2608.
- [58] U. Duh, G. Kosec, J. Slak, Fast variable density node generation on parametric surfaces with application to mesh-free methods, *SIAM Journal on Scientific Computing* 43 (2021) A980–A1000.
- [59] K. Sande, B. Fornberg, Fast variable density 3-d node generation, *SIAM Journal on Scientific Computing* 43 (2021) A242–A257.
- [60] G. Guennebaud, B. Jacob, et al., Eigen v3, <http://eigen.tuxfamily.org>, 2010.
- [61] E. Cuthill, J. McKee, Reducing the bandwidth of sparse symmetric matrices, in: *Proceedings of the 1969 24th national conference*, 1969, pp. 157–172.